AGU100 ADVANCING EARTH AND SPACE SCIENCE

Geochemistry, Geophysics, Geosystems

RESEARCH ARTICLE
10.1002/2017GC007152

Key Points:
- We develop an analytical multilayer poroelastic model to constrain the discharge zone permeability beneath a hydrothermal field
- We find that the poroelastic response to tidal loading is primarily controlled by layer 2A permeability
- Our estimated permeability structures reconcile the short-term response and long-term thermal output of hydrothermal sites

Correspondence to:
T. Barreyre,
thibaut.barreyre@uib.no

Citation:
Barreyre, T., Olive, J.-A., Crone, T. J., & Sohn, R. A. (2018). Depth-dependent permeability and heat output at basalt-hosted hydrothermal systems across mid-ocean ridge spreading rates. *Geochemistry, Geophysics, Geosystems*, *19*. https://doi.org/10.1002/2017GC007152

Received 21 JUL 2017
Accepted 24 FEB 2018
Accepted article online 12 MAR 2018

Depth-Dependent Permeability and Heat Output at Basalt-Hosted Hydrothermal Systems Across Mid-Ocean Ridge Spreading Rates

Thibaut Barreyre[1,2], Jean-Arthur Olive[3], Timothy J. Crone[4], and Robert A. Sohn[2]

[1]Department of Earth Science/K.G. Jebsen Centre for Deep Sea Research, University of Bergen, Bergen, Norway, [2]Woods Hole Oceanographic Institution, Woods Hole, MA, USA, [3]Laboratoire de Géologie, Ecole normale supérieure/CNRS UMR 8538, PSL Research University, Paris, France, [4]Lamont-Doherty Earth Observatory, Columbia University, Palisades, NY, USA

Abstract The permeability of the oceanic crust exerts a primary influence on the vigor of hydrothermal circulation at mid-ocean ridges, but it is a difficult to measure parameter that varies with time, space, and geological setting. Here we develop an analytical model for the poroelastic response of hydrothermal exit-fluid velocities and temperatures to ocean tidal loading in a two-layered medium to constrain the discharge zone permeability of each layer. The top layer, corresponding to extrusive lithologies (e.g., seismic layer 2A) overlies a lower permeability layer, corresponding to intrusive lithologies (e.g., layer 2B). We apply the model to three basalt-hosted hydrothermal fields (i.e., Lucky Strike, Main Endeavour and 9°46′N L-vent) for which the seismic stratigraphy is well-established, and for which robust exit-fluid temperature data are available. We find that the poroelastic response to tidal loading is primarily controlled by layer 2A permeability, which is about 3 orders of magnitude higher for the Lucky Strike site ($\sim 10^{-10}$ m^2) than the 9°46′N L-vent site ($\sim 10^{-13}$ m^2). By contrast, layer 2B permeability does not exert a strong control on the poroelastic response to tidal loading, yet strongly modulates the heat output of hydrothermal discharge zones. Taking these constraints into account, we estimate a plausible range of layer 2B permeability between $\sim 10^{-15}$ m^2 and an upper-bound value of $\sim 10^{-14}$ (9°46′N L-vent) to $\sim 10^{-12}$ m^2 (Lucky Strike). These permeability structures reconcile the short-term response and long-term thermal output of hydrothermal sites, and provide new insights into the links between permeability and tectonomagmatic processes along the global mid-ocean ridge.

1. Introduction

Circulation of hydrothermal fluids through young oceanic crust at mid-ocean ridges (MORs) accounts for up to ~10% of Earth's internal heat loss (Elderfield & Schultz, 1996; Sclater et al., 1980; Stein & Stein, 1992; Williams & Von Herzen, 1974), controls the thermo-mechanical state and degree of hydration of newly formed oceanic lithosphere (e.g., Emmanuel & Berkowitz, 2006; Iyer et al., 2010), profoundly affects the chemistry of the oceanic lithosphere and global ocean (e.g., Edmond et al., 1979; Elderfield & Schultz, 1996; Humphris et al., 1995; Wolery & Sleep, 1976), and provides a unique habitat for complex chemosynthetic ecosystems (e.g., Kelley et al., 2002; Lutz et al., 2008; Marcon et al., 2013; Nees et al., 2008; Shank et al., 1998). All of these hydrothermal systems processes are modulated by the permeability structure of the elastic matrix hosting fluid flow (e.g., Coumou et al., 2008; Driesner, 2010), which is a heterogeneous tensor field that varies in time and space, locally, and with geological context, globally. Constraining the matrix permeability structure is a fundamental problem for virtually all fields of hydrothermal research, but placing meaningful constraints on the parameters is technically difficult and often extremely costly (e.g., ocean drilling), which helps explain why permeability is probably the most poorly constrained hydrologic parameter for the oceanic crust (Fisher, 2004).

Direct in situ measurements (e.g., borehole packers) and indirect estimates and inferences (e.g., borehole temperatures, seafloor heat flow) for oceanic crust permeability are highly variable and span many orders of magnitude, with values as high as 10^{-11} m^2 near the seafloor to values lower than 10^{-18} m^2 at the base of the upper crust (e.g., Becker & Davis, 2003; Becker & Fisher, 2008; Davis et al., 2010; Fisher, 1998; Fisher et al., 2008; Winslow et al., 2013). The decreasing trend with depth is thought to reflect the closure of cracks and pores due to increasing lithostatic pressure and changes in crustal lithology. Although ocean crust permeability measurements and estimates from direct and indirect in situ methods vary widely, convection models of hydrothermal circulation at MORs suggest that the "effective permeability" of all discharge zones is in the range of 10^{-15}–10^{-12} m^2 (e.g.,

Coumou et al., 2008; Driesner, 2010; Hasenclever et al., 2014; Lowell & Germanovich, 2004; Lowell et al., 2013). The effective permeability represents the permeability that a single layer stretching between the magma chamber and the seafloor would have to have in order to match the thermo-chemical output observed at a hydrothermal field. The effective permeability thus represents an average in some sense over the entire layered crustal section between the magma chamber and the seafloor, immediately below the venting sites. It is noteworthy that the range of effective permeabilities estimated by Lowell et al. (2013) is considerably narrower than the variability documented by in situ measurements and indirect estimates. Therefore, the applicability of borehole measurements carried out mostly off-axis and at the sample scale is questionable for crustal-scale convection on-axis, where very few subseafloor in situ measurements have been made (Wilcock & Fisher, 2004).

These considerations have motivated a variety of innovative approaches for constraining matrix permeability over meaningful length scales and in young crust (e.g., Crone et al., 2011; Davis et al., 2010; Lowell & Germanovich, 2004; Theissen-Krah et al., 2011; Wilcock & Fisher, 2004; Wilcock & McNabb, 1996; Winslow et al., 2013), including the use of vent exit-fluid temperature and ocean tide (bottom pressure) time series data to model the poroelastic response of the matrix to tidal loading (Barreyre & Sohn, 2016; Barreyre et al., 2014a). These sorts of passive techniques that do not require sampling rocks from below the seafloor provide a cost-effective way to constrain permeability, but to this point it has been difficult to separate variability due to methods from that due to site-specific geology and hydrology.

In this paper, we investigate the permeability structure of the discharge zone of hydrothermal systems from a variety of geological settings on the global MOR system using two approaches. First, we develop a multilayer model for the poroelastic response to ocean tidal loading. We focus on the case of two layers of decreasing permeability with depth, which is consistent with the lithostratigraphy of volcanic crust formed at MORs. This approach allows us to compare the poroelastic response from sites with known and variable lithostratigraphies, and allows us to constrain the depth intervals over which the poroelastic response is controlled. Second, we attempt to reconcile our estimates of permeability layering with the observed heat output of hydrothermal sites using an analytical framework derived from Driesner (2010). Our analysis shows that the poroelastic response to ocean tidal loading is controlled by the permeability structure of extrusive layer 2A, which varies considerably across sites along the global MOR, while the effective permeability of the system and the efficiency of convective heat transfer is primarily controlled by the permeability structure of intrusive layer 2B. Taken together, these results improve our understanding of how the permeability structure for deep-sea hydrothermal systems varies across MOR spreading rates, and how it modulates the vigor of hydrothermal exchanges.

2. A Model for Tidal Modulation of Hydrothermal Systems With Depth-Dependent Permeability

We begin by presenting a 1-D model aimed at predicting the perturbations of the pressure, temperature, and velocity of fluids moving through a layered oceanic upper crust subjected to periodic fluctuations in seafloor pressure, imposed by tidal cycles (Figure 1). Our model is a generalization of the homogeneous permeability model of Jupp and Schulz (2004), and it extends the preliminary approach of Xu et al. (2017), who derived two-layer solutions for the phase lag of vent temperatures relative to tides but did not completely analyze the system behavior and solution space.

2.1. Fundamental Concepts and Equations of Poroelasticity

When a porous medium (e.g., the oceanic crust) is placed under an external load (e.g., ocean tides), the resulting stress is borne partly by the solid matrix and partly by the interstitial fluid, where it manifests as a change in fluid pressure, often referred to as a pore pressure perturbation. The partitioning of the total stress between the fluid and the solid matrix is a function of the elastic properties of the system and the porosity. It is thus possible for a locally uniform seafloor load to produce a time-periodic, spatially variable pressure perturbation field when there are gradients in these properties. The associated pressure gradients can drive interstitial fluid flow and perturb the background flow pattern (e.g., a hydrothermal convection cell). By perturbing the advection of mass and heat in regions of background fluid upwelling, the tidal forcing can, in principle, produce a phase lag between the loading function (seafloor pressure) and the velocity and temperature of the exit-fluids, which depends upon the poroelastic parameters of the system (e.g., Crone & Wilcock, 2005; Jupp & Schultz, 2004; Wang & Davis, 1996).

The equations governing the temporal (t) and spatial (z) evolution of pore pressure perturbation (p, departure from a reference pressure) within a porous, fluid-saturated domain consisting of N layers of uniform physical

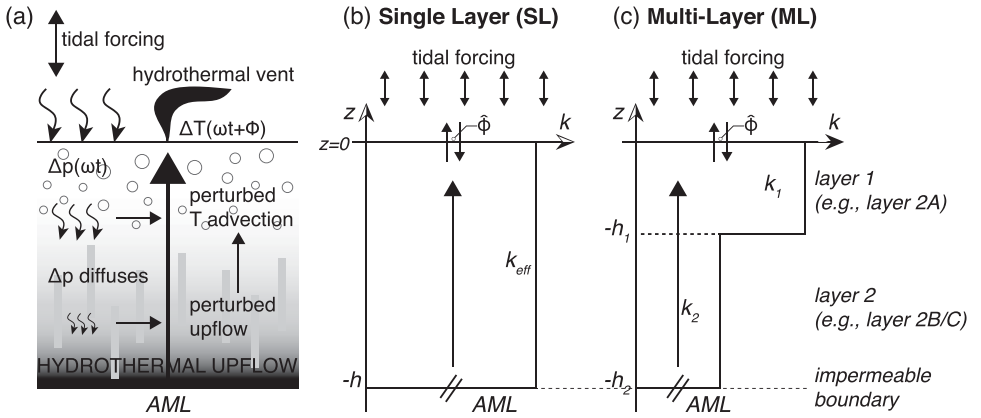

Figure 1. (a) Conceptual illustration of the perturbation exerted on hydrothermal upflow by tidal loading. (b, c) Setup of the 1-D poroelastic model used to relate the phase lag between vent temperatures and tides to the permeability of the oceanic crust. (b) Single-layer model (Jupp & Schulz, 2004); (c) two-layer model (this study). AML refers to the axial melt lens providing the heat to drive hydrothermal circulation.

properties (Biot, 1941; van der Kamp & Gale, 1983; Wang & Davis, 1996), and subjected to variations in surface load $\sigma_B(t)$ is:

$$\frac{\partial^2 p_j}{\partial z^2} = \frac{1}{\eta_j}\left(\frac{\partial p_j}{\partial t} - \gamma_j \frac{\partial \sigma_B}{\partial t}\right), \tag{1}$$

where the notation for this and subsequent equations is given in Table 1, and subscript j (j=1, 2, . . . , N − 1, N) refers to the properties of the jth layer, numbered downward. Parameters η and γ are the hydraulic diffusivity and loading efficiency, respectively. The hydraulic diffusivity is defined as:

$$\eta = \frac{k}{\mu S}, \tag{2}$$

where μ is the dynamic viscosity of the pore fluid, k is the permeability of the porous medium, and S is the uniaxial storage compressibility, defined as:

$$S = \left(K^{-1} - K_s^{-1}\right)\left(1 - \frac{4\psi}{3}\right) + \phi\left(K_f^{-1} - K_s^{-1}\right), \tag{3}$$

where K is the matrix drained bulk modulus, K_s is the solid grain bulk modulus, K_f is the fluid bulk modulus, ϕ is the porosity of the medium, and ψ is the dimensionless poroelastic stress coefficient (Detournay & Cheng, 1993). Detailed expressions for drained parameters K, determined by Gassmann's equation (Gassmann, 1951), and for dimensionless coefficient ψ are given in the Appendix A.

The loading efficiency γ is defined as:

$$\gamma = \frac{\beta(1+\nu)}{3(1-\nu) - 2\alpha\beta(1-2\nu)}, \tag{4}$$

where ν is the drained Poisson's ratio, α is the Biot-Willis parameter, and β is the Skempton's coefficient, all defined in the Appendix A.

Wang and Davis (1996) rewrite equation (1) in terms of an instantaneous pore pressure perturbation component $\left(p_j^i\right)$ and a diffusive pore pressure perturbation component $\left(p_j^d\right)$, which emphasizes the role γ and η play in characterizing the solution:

$$p_j^i = \gamma_j \sigma_B, \tag{5}$$

$$\frac{\partial p_j^d}{\partial t} - \eta_j \frac{\partial^2 p_j^d}{\partial z^2} = 0, \tag{6}$$

where

$$p_j = p_j^d + p_j^i. \tag{7}$$

Note that equation (6) has the form of a linear diffusion equation with diffusivity a piece-wise constant function of depth.

Table 1
Summary of Parameter Notations

a, b	2N complex coefficients.
A, B	Complex coefficients function of complex coefficients a and b and medium and fluid parameters.
C	Coefficient determined relative to the boundary condition on temperature perturbation.
D	Skin depth (m).
f	Tidal forcing frequency (s^{-1}).
g	Gravitational acceleration ($m.s^{-2}$).
G	Shear modulus (GPa).
h	Depth (m).
j	Subscript denoting properties in layer j ($j=1,2,\ldots,N-1,N$).
k	Permeability of the porous medium (m^2).
K	Matrix drained bulk modulus (GPa).
K_s	Solid grain bulk modulus (GPa).
K_f	Fluid bulk modulus (GPa).
I	Complex constant equal to $1+i$.
p	Pore pressure perturbation (Pa).
p^i	Instantaneous pore pressure perturbation component (Pa).
p^d	Diffusive pore pressure perturbation component (Pa).
p_T	Tidal loading function amplitude (Pa).
r	Ratio of heat capacities.
S	Uniaxial storage compressibility (Pa^{-1}).
t	Time (s).
T	Steady temperature (°C).
ΔT	Temperature perturbation (°C).
u	Vertical Darcy velocity perturbation ($m.s^{-1}$).
U	Steady Darcy velocity ($m.s^{-1}$).
V_P	P wave velocity ($m.s^{-1}$).
V_S	S wave velocity ($m.s^{-1}$).
z	Vertical coordinate (m).
α	Biot-Willis parameter.
β	Skempton's coefficient.
γ	Loading efficiency.
Γ	Background temperature gradient ($°C.m^{-1}$).
η	Hydraulic diffusivity ($m^2.s^{-1}$).
μ	Dynamic viscosity of the pore fluid (Pa.s).
ν	Drained Poisson's ratio.
ρ	Bulk density ($kg.m^{-3}$).
ρ_f	Fluid density ($kg.m^{-3}$).
ρ_s	Rock density ($kg.m^{-3}$).
ρ_{sw}	Seawater density ($kg.m^{-3}$).
σ_B	Loading function (e.g., oceanic tides) (Pa).
ϕ	Porosity of the medium.
φ	Phase angle (°).
ψ	Dimensionless poroelastic stress coefficient.
ω	Angular frequency of tidal forcing ($rad.s^{-1}$).

2.2. Analytical Solutions for 1-D Multilayer (and Multifrequency) Model

In the following subsections, we outline the general solution for each parameter of interest in layer j, namely: pore pressure perturbation, vertical velocity, and temperature. These solutions rely on generic coefficients (e.g., a_j, b_j, A_j, B_j, and C_j) that are determined by applying appropriate boundary conditions (BCs) to equation (6).

2.2.1. Pore Pressure

Tidal loading at the seafloor can be described as a periodic function of time:

$$\sigma_B(t)=p_T e^{i\omega t}, \tag{8}$$

where p_T and ω are the amplitude and angular frequency of the tidal loading (e.g., corresponding to a 12 and 24 h period for the M2 and K1 tides, respectively). With this type of harmonic forcing, the solution for pore pressure perturbation $\left(p_j(z,t)\right)$ in a multilayer system can be written:

$$p_j(z,t)=\left[a_j e^{I.\pi.z/D_j}+b_j e^{-I.\pi.z/D_j}+\gamma_j\right]p_T e^{i\omega t}, \tag{9}$$

where I is a complex constant equal to $1+i$, and D is the skin depth defined as

$$D_j=\sqrt{\frac{\pi\eta_j}{f}}, \tag{10}$$

and a_j and b_j denote $2N$ complex coefficients. These are determined using the Fourier-transformed BCs, which involves solving a system of $2N$ complex algebraic equations. In the simplest case with $N=2$ (Figure 1), BCs for the pore pressure perturbation solution (equation (9)) are:

1. $p_1^d(0,t)=(1-\gamma_1)\sigma_B$,
2. Continuity of pressure across layers: $p_1^d(-h_1,t)+\gamma_1\sigma_B=p_2^d(-h_1,t)+\gamma_2\sigma_B$,
3. Continuity of velocities across layers: $\frac{k_1}{\mu_1}\frac{\partial p_1^d}{\partial z}\Big|_{z=-h_1}=\frac{k_2}{\mu_2}\frac{\partial p_2^d}{\partial z}\Big|_{z=-h_1}$
4. $\frac{\partial p_2^d}{\partial z}\Big|_{z=-h_2}=0$,

where h_1 and h_2 denote the depth to the bottom of layers 1 and 2, respectively. The corresponding system of complex algebraic equations (combination of BCs and equation (9)) writes:

$$\begin{bmatrix} 1 & 1 & 0 & 0 \\ e^{-I\pi h_1/D_1} & e^{I\pi h_1/D_1} & -e^{-I\pi h_1/D_2} & -e^{I\pi h_1/D_2} \\ \frac{I\pi}{D_1}\frac{k_1}{\mu_1}e^{-I\pi h_1/D_1} & -\frac{I\pi}{D_1}\frac{k_1}{\mu_1}e^{I\pi h_1/D_1} & -\frac{I\pi}{D_2}\frac{k_2}{\mu_2}e^{-I\pi h_1/D_2} & \frac{I\pi}{D_2}\frac{k_2}{\mu_2}e^{I\pi h_1/D_2} \\ 0 & 0 & e^{-I\pi h_2/D_2} & -e^{I\pi h_2/D_2} \end{bmatrix} \cdot \begin{bmatrix} a_1 \\ b_1 \\ a_2 \\ b_2 \end{bmatrix} = \begin{bmatrix} 1-\gamma_1 \\ \gamma_2-\gamma_1 \\ 0 \\ 0 \end{bmatrix}.$$

The complex coefficients a_1, b_1, a_2, and b_2 are then determined by solving the two complex algebraic equations systems above using MATLAB's Symbolic Math Toolbox.

2.2.2. Velocity

The perturbation in vertical fluid velocity $\left(u_j(z,t)\right)$ due to tidal loading can be modeled as a Darcy velocity driven by gradients in pore pressure perturbation (p_j):

$$u_j(z,t)=-\frac{k_j}{\mu}\frac{\partial p_j}{\partial z}. \tag{11}$$

The analytical solution for velocity in a multilayer system is obtained through a spatial derivative of equation (9):

$$u_j(z,t)=-\frac{k_j I\pi}{\mu D_j}\left(a_j e^{I.\pi.z/D_j}-b_j e^{-I.\pi.z/D_j}\right)p_T e^{i\omega t}. \tag{12}$$

Note that the velocity perturbation at the seafloor ($z=0$) is of particular interest since it can be measured by seafloor instruments such as a direct flow meter (e.g., Germanovich et al., 2015) or camera systems that use image analysis methods (e.g., Crone et al., 2010; Mittelstaedt et al., 2010, 2012, 2016). It is expressed as:

$$u_1(0,t)=-\frac{k_1 I\pi}{\mu D_1}\left(a_1-b_1\right)p_T e^{i\omega t}. \tag{13}$$

The phase lag of the velocity perturbation at the seafloor $(u_1(0,t))$ relative to the tidal loading at the seafloor $(\sigma_B(t))$ is given by:

$$\Delta\varphi_u = arg(u_1(0,t)) - arg(\sigma_B(t))[\pm 2n\pi], \tag{14}$$

where n can be any integer.

2.2.3. Temperature

So far, we have considered the pore pressure change $(p_j(z,t))$ and velocity perturbation $(u_j(z,t))$ due to tidal loading. However, recording time series of these quantities at the seafloor (i.e., in hydrothermal vent exit fluids) is technically challenging. By contrast, it is much simpler to measure temperature fluctuations in fluids discharging at the seafloor $(\Delta T_1(0,t))$ (e.g., Barreyre & Sohn, 2016; Barreyre et al., 2014a, 2014b; Fornari et al., 1998; Larson et al., 2009; Lilley et al., 2003; Scheirer et al., 2006; Sohn, 2007; Tivey et al., 2002). We therefore complement our previous solutions with an analytical expression for temperature fluctuations due to tidal loading $(\Delta T_j(z,t))$.

Our assumption of 1-D geometry means that we must ignore lateral flow and instead consider the idealized case of uniform vertical flow across the permeable layers, which is an acceptable approximation for a region of hydrothermal upwelling that underlies seafloor vent fields. We define a characteristic vertical velocity U_j and temperature T_j for the background upwelling flow that is perturbed by tidal loading, and introduce corresponding perturbation quantities (u_j and ΔT_j, respectively). We further assume a linear background (steady) temperature $T_j = T_0 - \Gamma_j z$, with Γ the background temperature gradient (Jupp & Schultz, 2004), and approximate the steady upwelling velocity as $U_j = \frac{k_j}{\mu_j}(\rho_{sw} - \rho_f)g$, where ρ_{sw} is the density of background seawater and ρ_f the hydrothermal fluid density.

Assuming that tidally induced changes in the fluid density and adiabatic cooling are negligible, the advection of temperature under tidal loading is expressed as:

$$\frac{\partial(T_j + \Delta T_j)}{\partial t} + r(U_j + u_j)\frac{\partial(T_j + \Delta T_j)}{\partial z} = -r\Gamma_j U_j, \tag{15}$$

where the right side represents a 1-D approximation of the rate at which upwelling fluids are cooled conductively and adiabatically (Jupp & Schultz, 2004). This equation can be linearized and rewritten as:

$$\frac{\partial \Delta T_j}{\partial z} + \frac{1}{rU_j}\frac{\partial \Delta T_j}{\partial t} = \frac{\Gamma_j}{U_j}\, u_j\,. \tag{16}$$

Assuming that the velocity perturbation solution is given by equation (12), we solve equation (16) and express the solution for temperature perturbation as follows:

$$\Delta T_j(z,t) = C_j e^{-\frac{i\omega}{rU_j}z} e^{i\omega t} + A_j e^{\frac{l\pi z}{D_j}} + B_j e^{\frac{-l\pi z}{D_j}}, \tag{17}$$

where A_j and B_j are two complex coefficients written as functions of the complex coefficients a_j and b_j defined earlier, and of various medium/fluid parameters:

$$A_j = -\frac{\Gamma_j k_j l\pi}{U_j \mu_j D_j}\,\frac{1}{\frac{l\pi}{D_j} + \frac{i\omega}{rU_j}}\; p_T e^{i\omega t} a_j$$

and

$$B_j = +\frac{\Gamma_j k_j l\pi}{U_j \mu_j D_j}\,\frac{1}{\frac{-l\pi}{D_j} + \frac{i\omega}{rU_j}}\; p_T e^{i\omega t} b_j.$$

The third coefficient C_j is determined using the following BCs for temperature perturbation (equation (17)):

- $\Delta T_1(-h_1,t) = \Delta T_2(-h_1,t)$
- $\Delta T_2(-h_2,t) = 0.$

For the two-layer case with an impermeable lower boundary at $z = -h_2$, the C coefficients are:

$$C_1 = \left[-e^{\frac{i\omega}{rU_2}(h_1 - h_2)} \left(A_2 e^{\frac{-I\pi h_2}{D_2}} + B_2 e^{\frac{I\pi h_2}{D_2}} \right) + A_2 e^{\frac{-I\pi h_1}{D_2}} + B_2 e^{\frac{I\pi h_1}{D_2}} - A_1 e^{\frac{-I\pi h_1}{D_1}} - B_1 e^{\frac{I\pi h_1}{D_1}} \right] \times e^{-\frac{i\omega}{rU_1} h_1} e^{-i\omega t}$$

and

$$C_2 = -e^{-\frac{i\omega}{rU_2} h_2} \left(A_2 e^{\frac{-I\pi h_2}{D_2}} + B_2 e^{\frac{I\pi h_2}{D_2}} \right) e^{-i\omega t}.$$

The two-layer temperature perturbation at the seafloor $(\text{i.e., } \Delta T_1(0,t) = C_1 + A_1 + B_1)$ is then obtained by inserting expressions of C_1, A_1, and B_1 in equation (17), where z = 0. This yields:

$$\Delta T_1(0,t) = \left[C_1 - \frac{\Gamma_1 k_1 I\pi}{U_1 \mu_1 D_1} \left(\frac{1}{\frac{I\pi}{D_1} + \frac{i\omega}{rU_1}} a_1 + \frac{1}{\frac{-I\pi}{D_1} + \frac{i\omega}{rU_1}} b_1 \right) \right] p_T e^{i\omega t}. \tag{18}$$

Further, the phase lag of the temperature fluctuation at the seafloor $(\Delta T_1(0,t))$ relative to the ocean tide $(\sigma_B(t))$ is given by:

$$\Delta\varphi_T = arg(\Delta T_1(0,t)) - arg(\sigma_B(t)) \ [\pm 2n\pi], \tag{19}$$

where n can be any integer. This solution for phase lag is of particular interest and will be used in the remainder of this study to infer permeability layering in real systems, using time series of seafloor vent temperatures. Before doing so, however, we briefly describe how this phase lag varies as a function of layer geometry and permeability. In the following, we restrict ourselves to the two-layer case, which is appropriate for typical upper oceanic crust comprising an upper layer (2A, $j = 1$ in Figure 1) of extrusives and a lower layer (2B, $j = 2$ in Figure 1) of sheeted dikes. Figure 2b provides an example solution of phase lag $\Delta\varphi_T$ as a function of k_{2A} and k_{2B}, and compares it to the single layer solution (Figure 2a).

2.3. Effect of Heterogeneous Permeability

In order to gain insight into the underlying physics of poroelastic modulation due to periodic loading in a two-layer system, we define four distinct system behaviors (regimes in Figure 2c), which depend on both the permeability (k_{2A}, k_{2B}) and geometry of the layers (thicknesses H_{2A}, H_{2B}), as follows:

1. **Regime 1 (R1)** corresponds to low permeabilities in layer 2B, and a wide range of permeabilities in layer 2A. Low permeability makes layer 2B behave as an impermeable boundary at the base of 2A, which effectively decouples the two layers. This regime is thus analogous to a shallow single-layer system where the poroelastic behavior is entirely controlled by the layer 2A thickness and permeability (Figures 2a and 2b).
2. **Regime 2 (R2)**: Wide, intermediate range of permeabilities for both layer 2A and 2B. This transitional regime describes a system where the overall poroelastic behavior reflects strong coupling between the parameters of both layers, and maps in (k_{2A}, k_{2B}) space (Figure 2c) as a "funnel-shaped" pattern in phase lag contours. Layer geometry exerts a strong modulation on this pattern (not shown in Figure 2c). The lower the ratio of H_{2A}/H_{2B} (i.e., H_1/H_2 in Figure 2c), the more the funnel-shaped phase lag pattern is pushed toward greater layer 2A permeabilities, and vice versa. Thicker H_{2B} (i.e., H_2 in Figure 2c) shifts the funnel-shaped pattern toward greater layer 2B permeabilities, and vice versa.
3. **Regime 3 (R3)**: Layer 2A and 2B have relatively similar, high permeability. This regime describes a uniform system where the poroelastic behavior is therefore controlled by the uniform permeability of layer 2A and 2B, as well as the overall thickness of the system, following the single layer solutions of Jupp and Schulz (2004).
4. **Regime 4 (R4)**: A wide range of permeabilities for Layer 2B, and high permeabilities for layer 2A. Layer 2A has such a high permeability that it poses no resistance to the tidal modulation (signals diffuse through it very efficiently). This manifests as a decoupling of the two layers where a "ghost" layer 2A has very little influence. This regime describes a system where the poroelastic behavior is therefore controlled by the permeability and thickness of layer 2B.

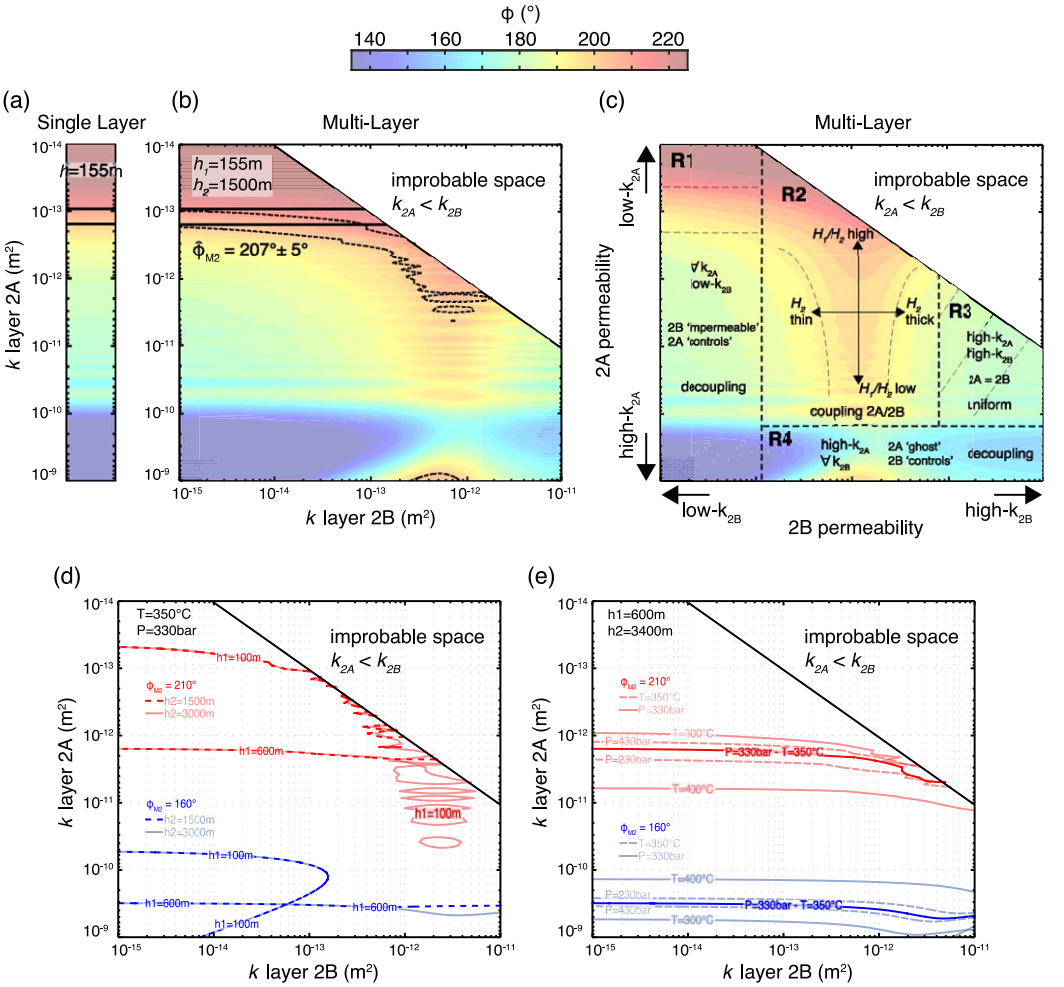

Figure 2. Controls on the phase lag between vent temperatures and M2 tides. (a) In a single layer (2A) of thickness 155 m, a phase lag of 207° requires a permeability of $\sim 10^{-13}$ m^2 (thick contours). (b) By contrast, in a two-layer model of total thickness 1,500 m, the same phase lag requires a specific combination of layers 2A and 2B permeabilities. The two-layer model asymptotes the single-layer model as k_{2B} decreases. (c) Typical phase lag map illustrating the four key regimes (R1–R4) described in section 2.3. (d) Sensitivity of 2 phase lag contours (210° in red and 160° in blue) to changes in the thickness of the layers. (e) Sensitivity of the same contours to changes in the assumed average pressure and temperature that set the thermodynamic properties of the fluid in both layers (see section 2.3).

This basic exploration of parameter space demonstrates that combining knowledge of the crustal structure (e.g., H_{2A} and H_{2B} from seismic profiles) with phase lag estimated between time series of in situ exit-fluid temperature and tidal pressure can place strong constraints on the poroelastic regime experienced by the layered system, and therefore on its first-order permeability structure.

While permeability controls the temperature-tide phase lag to first order, Figures 2d and 2e further explore the sensitivity of phase lag to the geometry of the system (i.e., layer 2A and 2B thickness–Figure 2d) and the thermodynamic properties of the fluids (primarily modulated by the temperature and pressure of the fluid–Figure 2e, Table 2). This is done over a large range of layer 2A and 2B permeability spanning 6 orders of magnitude. In Figures 2d and 2e, we specifically outline the combinations of (k_{2A}, k_{2B}) that can explain two phase lag values: 210° (red) and 160° (blue), which represent two commonly observed values of phase lag reported by Barreyre and Sohn (2016). Different line shading and shapes represent different model assumptions (e.g., different fluid temperature/pressure, or layer 2A/2B thickness), which are detailed in the caption of Figures 2d and 2e. Figure 2d shows the relative importance of the geometry of the system in controlling the phase lag under fixed fluid temperature and pressure. In particular, the thickness of layer 2A exerts an important control on phase lag, and increasing H_{2A} from 100 to 600 m (with every other parameter fixed)

Table 2
Baseline Fluid and Poroelastic Parameters

Fluid and poroelastic parameters	Symbols	Values	
M_2 tidal angular frequency	ω_{M2} (rad s^{-1})	1.408×10^{-4}	
K_1 tidal angular frequency	ω_{K1} (rad s^{-1})	7.2921×10^{-5}	
Density of seawater	ρ_0 (kg m^{-3})	1,047.3[a]	
Density of hydrothermal fluids	ρ_f (kg m^{-3})	700.5[b]	
Fluid viscosity	μ (Pa s)	7.9×10^{-5}[c]	
		Layer 2A	Layers 2B/2C
Ratio of heat capacities	R	1.5	1.3
P wave velocity	V_p (m s^{-1})	2,200[d]	5,500[e]
S wave velocity	V_s (m s^{-1})	431	2,940
Porosity	Φ	0.2[f]	0.03[g]
Bulk density	ρ (kg m^{-3})	2,500.1	2,882.5
Grain bulk modulus	K_g (GPa)	50[h]	70[i]
Fluid bulk modulus	K_f (GPa)	0.29[j]	0.29[j]
Matrix (drained) bulk modulus	K_m (GPa)	10.6	53.4
Storage compressibility for 1-D loading	S_1 (Pa^{-1})	7.46×10^{-10}	1.05×10^{-10}

[a]Density of seawater calculated for pressure at 330 bar and background seawater temperature at 3°C; from Holzbecher (1998); Rabinowicz et al. (1999); and Fontaine et al. (2001). [b]Density of hydrothermal fluids calculated for pressure at 330 bar and hydrothermal fluid temperature at 350°C; from Holzbecher (1998); Rabinowicz et al. (1999); and Fontaine et al. (2001). [c]Calculated for hydrothermal fluid temperature at 350°C; from Fontaine et al. (2001). [d]Sohn et al. (2004). [e]Vera et al. (1990). [f]Luyendyk (1984). [g]Becker (1985). [h]Carmichael (1966) and Christensen and Salisbury (1972). [i]Pros et al. (1962). [j]Computed from the equations of state for pressure at 330 bar and hydrothermal fluid temperature at 350°C.

can significantly change the values of (k_{2A}, k_{2B}) required to explain a given phase lag, primarily toward greater values of k_{2A} (by up to 2 orders of magnitude) with small changes in k_{2B}. Figure 2e illustrates the effect of fluid properties on phase lag for a fixed system geometry. The combinations of (k_{2A}, k_{2B}) that are required to explain a given phase lag appear less sensitive to changes in fluid properties, as they change by less than 1 order of magnitude, when pressure-temperature conditions are varied within a reasonable range. Greater sensitivity is observed for temperatures approaching 400°C, which reflects the high sensitivity of fluid properties to changes in temperature and pressure near the triple point of water.

In summary, layer permeability and thickness, particularly in layer 2A (i.e., H_{2A} and k_{2A}), control the temperature phase lag to first order, while fluid properties exert a second-order control. This exploration of parameter space gives us confidence that if layer geometry is well constrained by seismological techniques, measurements of temperature-tide phase lags can be used to constrain combinations of layers 2A and 2B permeabilities within ~1 order of magnitude, and that greater phase lags generally provide a more robust constraint on k_{2B}.

3. Available Data Sets of Exit-Fluid Temperature and Pressure Lags

3.1. Obtaining Estimates of Temperature-Tide Phase Lags

We use the phase lag estimates for exit-fluid high temperature versus tidal pressure published by Barreyre and Sohn (2016) as the basis for our analyses. These phase lag estimates represent the most robust values obtained from a comprehensive analysis of the complete set of publicly available (Marine Geoscience Data System, PANGAEA, European Multidisciplinary Seafloor and water column Observatory, and Ocean Networks Canada) exit-fluid high-temperature time series data for vents at the Lucky Strike Hydrothermal Field (LSHF), the Main Endeavour Field (MEF), and the East Pacific Rise (EPR) 9°46′N sites (e.g., Barreyre et al., 2014b; Fornari et al., 1998; Larson et al., 2009; Scheirer et al., 2006; Tivey et al., 2002). These hydrothermal sites are located on MORs spanning a large range of spreading rates, from slow to fast (MAR: 2.2 cm yr^{-1} (Cannat et al., 1999); JdFR: 6 cm yr^{-1} (Riddihough, 1984); EPR: 11 cm yr^{-1} (Carbotte & Macdonald, 1994)). Coherency and phase lag between tidal pressure at the seafloor (i.e., data generated with the GOT4.7 global ocean tide model (Ray, 2013) as described in Barreyre & Sohn, 2016), and exit-fluid high temperatures are estimated by applying multitaper (Thomson, 1982) cross-spectral methods with adaptive weighting (Percival & Walden, 1993) to time series data (see details in Barreyre & Sohn, 2016). After applying stringent

Table 3
Average Phase Lag ($\hat{\phi}$) and Errors ($\bar{e}_{\hat{\phi}}$) Estimates at M2 Semidiurnal Frequency and K1 Diurnal Frequency Estimated From Spectral Analysis Following the Methodology Described in Barreyre and Sohn (2016*)*

Hydrothermal fields		$\hat{\phi}_{M2}$(°)	$\bar{e}_{\hat{\phi}_{M2}}$(°)	$\hat{\phi}_{K1}$(°)	$\bar{e}_{\hat{\phi}_{K1}}$(°)	H_{2A} (m)	H_{2B} (m)	k_{2A} (m^2)	k_{2B} (m^2)
LSHF	***West***	155	5			300[b]	3,400[c]	$\sim 1.5 \times 10^{-10} - 10^{-9}$	$\sim 10^{-15} - 1.5 \times 10^{-12}$
(MAR)	***East***	173	4	*168*[a]	*7*[a]	600[b]		$\sim 7 \times 10^{-11} - 2 \times 10^{-10}$	$\sim 10^{-15} - 5 \times 10^{-13}$
MEF	***South (S&M)***	178.5	1.5	160	5	460[d]	2,300[d]	$\sim 1.5 \times 10^{-10}$	$\sim 10^{-15} - 1.5 \times 10^{-13}$
(JdFR)	***North (Grotto)***	217	2.5	201	4			$\sim 6 \times 10^{-13} - 8 \times 10^{-13}$	$\sim 10^{-15} - 7 \times 10^{-14}$
9°50′N Field	***L-vent***	207	5	188	7	155[e]	1,500[f]	$\sim 1.5 \times 10^{-13} - 2.5 \times 10^{-13}$	$\sim 10^{-15} - 2 \times 10^{-14}$
(EPR)									

Note. Phase lag angles are estimated for coherency $(\gamma^2) \geq 0.85$ at the M2 frequency for LSHF, MEF, and EPR and at the K1 frequency for MEF and EPR; and for coherency $(\gamma^2) \geq 0.7$ at the K1 frequency for LSHF.
[a]Estimated for lower coherency $(\gamma^2) \geq 0.7$. [b]Arnulf et al. (2011). [c]Singh et al. (2006); Crawford et al. (2013). [d]Van Ark et al. (2007). [e]Sohn et al. (2004). [f]Detrick et al. (1987).

criteria for phase analysis (e.g., coherency $(\gamma^2) \geq 0.85$) to maximize the signal-to-noise ratio, Barreyre and Sohn (2016) provided a highly coherent and stable data set of phase lag estimates consisting of two records (∼2.4 years of recording) for the EPR-9°46′N, 30 records (∼27 years of recording) for the LSHF, and two records (∼0.8 years of recording) for the MEF. The corresponding average values of phase lag and the associated uncertainty for each site/time series are listed in Table 3.

3.2. Background Information on the Hydrothermal Sites From Our Compilation

3.2.1. East Pacific Rise 9°50′N Field (EPR-9°50′N)

The 9°50′N hydrothermal field is located on a volcanically active segment of the fast-spreading EPR (11 cm yr^{-1}, Carbotte & Macdonald, 1994) that has experienced recent volcanic/magmatic activity in 1991 (Haymon et al., 1993; Rubin et al., 1994), 2005–2006 (Tolstoy et al., 2006), and possibly in 1995 (Germanovich et al., 2011). Because a considerable amount of seismic work has been carried out at the EPR (e.g., Detrick et al., 1987; Sohn et al., 2004; Xu et al., 2014), we have reliable constraints on the depth of the axial melt lens (AML) beneath the hydrothermal field (∼1,500 m, Detrick et al., 1987) and on the relatively low thickness of layer 2A (∼150 m, Christeson et al., 1996; Harding et al., 1993; Sohn et al., 2004; Vera & Diebold, 1994). We have phase lag data for a specific vent within the 9°50′N field: L-vent. Cross-spectral analysis yields phase lag estimates at this vent of 207° ± 5° at M2 frequency and 188° ± 7° at K1 frequency (Barreyre & Sohn, 2016).

3.2.2. Lucky Strike Hydrothermal Field (LSHF)

The Lucky Strike hydrothermal field is located above a volcanic center on the slow-spreading Mid-Atlantic Ridge (MAR, 2.2 cm yr^{-1}; Cannat et al., 1999), and provides the most extensive set of hydrothermal discharge time series data acquired to date. Seismic studies have also provided strong constraints for both the magma chamber depth (∼3,400 m) and the thickness of the extrusive layer 2A (∼600 m) (Arnulf et al., 2011; Crawford et al., 2013; Seher et al., 2010; Singh et al., 2006). It has been shown that there exists a difference in phase lag between vents located on the west (155° ± 5° at M2 frequency—no estimate at K1 frequency) versus the east (173° ± 4° at M2 frequency and 168° ± 7° at K1 frequency) side of the LSHF (Barreyre & Sohn, 2016). The two sets of vents are separated by a solidified lava lake (∼ 300 m in diameter) that forms an impermeable cap on the extrusive layer (Barreyre et al., 2012; Fouquet et al., 1995; Ondréas et al., 2009). Note that we had to lower the coherency threshold to $(\gamma^2) \geq 0.7$ at the K1 frequency for LSHF-E in order to obtain a phase lag estimate. While less stringent than in all other sites of the compilation, this criterion still ensures a coherent and stable result.

3.2.3. Main Endeavour Field (MEF)

The Main Endeavour Field is located on the intermediate-spreading Juan de Fuca Ridge (JdFR, 6 cm yr^{-1}; Riddihough, 1984) at 47°N. Seismic studies provide estimates for both the magma chamber depth (∼2,300 m) and the extrusive layer 2A thickness (∼460 m) (Van Ark et al., 2007). Intrafield variability is also evident at the MEF, where the Grotto site exhibits phase lags of 217° ± 2.5° at M2 frequency (and 201° ± 4° at K1), which exceeds the phase lag at the S&M site by ∼40° (178.5° ± 1.5° at M2 frequency and 160° ± 5° at K1). These differences are much larger than the phase lag uncertainties and intersite variability, indicating that they arise from deterministic differences in the subsurface permeability structure.

4. Results

It is important to note that the permeabilities estimated below and discussed throughout this paper are interpreted as corresponding specifically to discharge zone permeabilities, and therefore, cannot be interpreted as whole crustal permeabilities. In layer 2A the flow to a vent field is likely the result of flow within a limited volume and thus, may not be representative of layer 2A as a whole (Cann & Strens, 1989; Fontaine et al., 2007), since the very presence of the vent field could result from an anomalously permeable underlying crust (e.g., Crone et al., 2011).

4.1. Inverting for Discharge Zone Permeability Layering at Hydrothermal Fields

Using the model described above, we computed the predicted phase lag of vent temperature relative to tidal pressure at the seafloor as a function of the permeabilities of layer 2A and 2B (Figure 3). We assumed that the respective thickness of the layers beneath each hydrothermal site was known from previous seismic studies summarized in the previous section, and in Table 3. We then used our phase lag estimates at both the M2 and K1 frequencies to constrain the model and reduce the permissible solution space to narrow contours (black contours in Figure 3) for each site.

Figure 3 highlights a key dichotomy previously reported by Barreyre and Sohn (2016), between high layer 2A permeability systems ($k_{2A} > \sim 10^{-11}$ m^2: LSHF-W and LSHF-E and MEF-S&M), and low layer 2A permeability systems ($k_{2A} < \sim 10^{-11}$ m^2: EPR-Lvent and MEF-Grotto). Our two-layer model, however, reveals previously unknown effects due to coupling with a less permeable layer 2B (e.g., bending of the solution contour for higher layer 2B permeability). Overall, we find that the phase lag between exit-fluid temperature and tidal loading is relatively insensitive to the permeability of layer 2B, with the range of permeabilities that fit the phase lag data spanning several orders of magnitude (i.e., up to 3).

In order to further constrain our permeability estimates, we only retained combinations of (k_{2A}, k_{2B}) that could jointly explain the observed phase lag at both the M2 and K1 tidal frequencies (except for LSHF-W, where robust phase lag estimates at the K1 frequency could not be obtained). Final constrained permeability ranges for layers 2A and 2B are shown in Figure 4 and summarized in Table 3. Our estimates are in broad agreement with previous studies, but provide further insight into the systematic variability of permeability layering at MOR hydrothermal sites (Figure 4b).

At the EPR, where the base of layer 2A is located at the relatively shallow depth of ~155 mbsf (Sohn et al., 2004), the phase lag estimates for L-vent (207°±5° @ M2 and 188°±7° @ K1) require a permeability for layer 2A ranging from $\sim 1.5 \times 10^{-13}$ to 2.5×10^{-13} m^2 and from $\sim 10^{-15}$ to 2×10^{-14} m^2 for layer 2B.

By contrast, at the LSHF the smaller phase lags (155° ± 5° @ M2 for LSHF-W and 173° ± 4° @ M2 and 168° ± 7° @ K1 for LSHF-E) require a much higher effective permeability for layer 2A ranging from $\sim 1.5 \times 10^{-10}$ to 10^{-9} m^2 for LSHF-W and $\sim 7 \times 10^{-11}$ to 2×10^{-10} m^2 for LSHF-E. They also constrain layer 2B permeability between $\sim 10^{-15}$ and 1.5×10^{-12} m^2 for LSHF-W and between $\sim 10^{-15}$ and 5×10^{-13} m^2 for LSHF-E.

Intermediate behaviors are observed at the MEF where the extrusive layer thickness is ~450 m (Van Ark et al., 2007). At Grotto vent, the phase lags of 217° ± 2.5° @ M2 and 201° ± 4° @ K1 require an effective permeability ranging from $\sim 6 \times 10^{-13}$ to 8×10^{-13} m^2 for layer 2A and from $\sim 10^{-15}$ to 7×10^{-14} m^2 for layer 2B, whereas the smaller phase lags observed for S&M vent (178.5° ± 1.5° @ M2 and 160° ± 5° @ K1) require an effective permeability of $\sim 1.5 \times 10^{-10}$ m^2 for layer 2A and ranging from $\sim 10^{-15}$ to 1.5×10^{-13} m^2 for layer 2B.

Note that the estimated permeability ranges above are bounded by a minimum permeability of 10^{-15} m^2 for layer 2B. This cutoff permeability of 10^{-15} m^2 is an outcome of the coupling between layers in our model, and corresponds to the minimum permeability at which layer 2B exerts some influence on the observed phase lag. For any lower k_{2B}, layer 2B becomes too impermeable and the model behaves like a single-layer, homogenous model with an effectively impermeable boundary at the base of layer 2A (Figures 2a and 2b). In section 5.3, we propose a lower bound on k_{2B} using heat flow constraints.

4.2. Effect of Layer Thickness on the Poroelastic Response at the Field Scale

In the previous section, we estimated the permeability structure for several hydrothermal fields that have well-constrained layer thicknesses from seismic studies. Here, we focus on variability within individual fields, and the potential contribution of changes in layer 2A/2B thickness to this variability. At the LSHF, the difference in phase lags estimated for the western (155° ± 5° @ M2 for LSHF-W) versus eastern

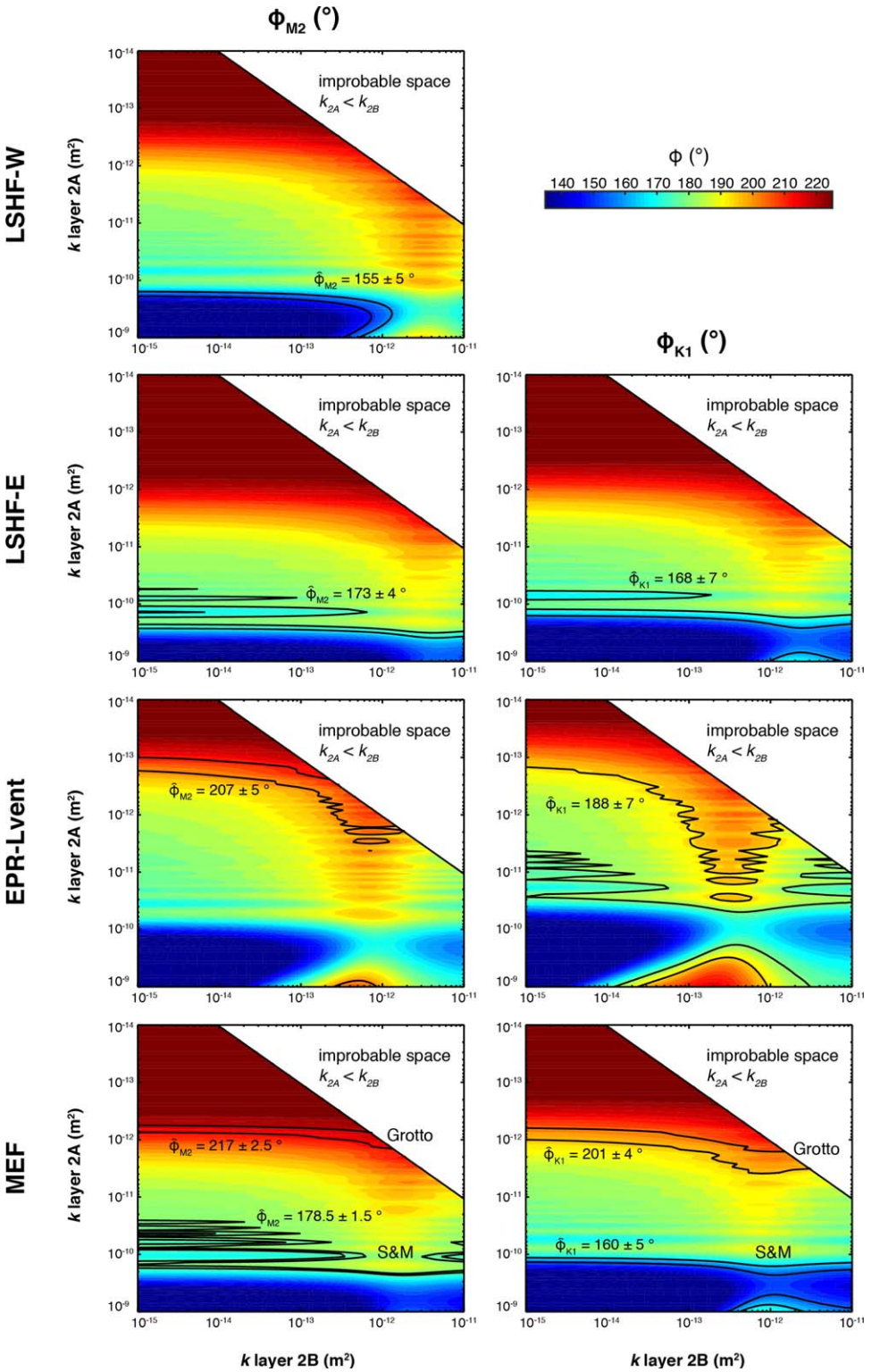

Figure 3. Contours of measured phase lags at the Lucky Strike Hydrothermal field (LSHF, Western and Eastern vents), the East Pacific Rise (EPR, L-vent), and the Main Endeavour Field (MEF, S&M, and Grotto vents), plotted as a function of k_{2A} and k_{2B} assuming layers 2A and 2B geometries summarized in Table 3. The left and right columns correspond to M2 and K1 tidal frequencies, respectively.

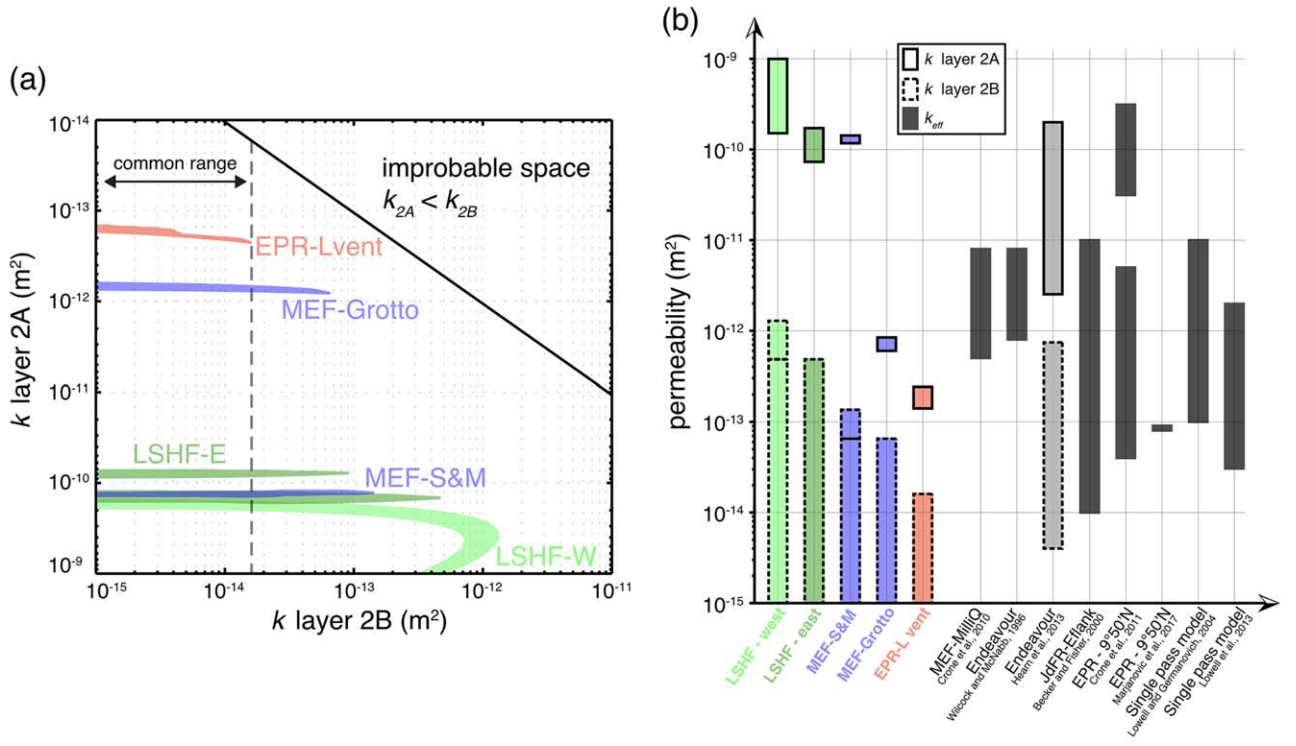

Figure 4. (a) Combined constraints on layers 2A and 2B permeability for each site obtained by combining phase lag data at M2 and K1 frequencies, whenever available. (b) Synthesis of our results compared with permeability estimates from previous studies. k_{eff} denotes an effective permeability that is not explicitly tied to either layers 2A nor 2B permeabilities.

(173° ± 4° @ M2 and 168° ± 7° @ K1 for LSHF-E) vents is consistent with a change in the extrusive layer thickness that has been imaged seismically (300 m for the west vents versus 600 m for the east vents, Arnulf et al., 2011). Figure 5 shows the effect of layer 2A thickness on the M2 phase lag assuming a permeability of 10^{-14} m^2 in layer 2B and a range of permeabilities for layer 2A. Systematic phase lag differences are observed between vent sites hosted on the east versus west side of the LSHF, which can be explained entirely by a change in 2A thickness and requires no change in 2A permeability.

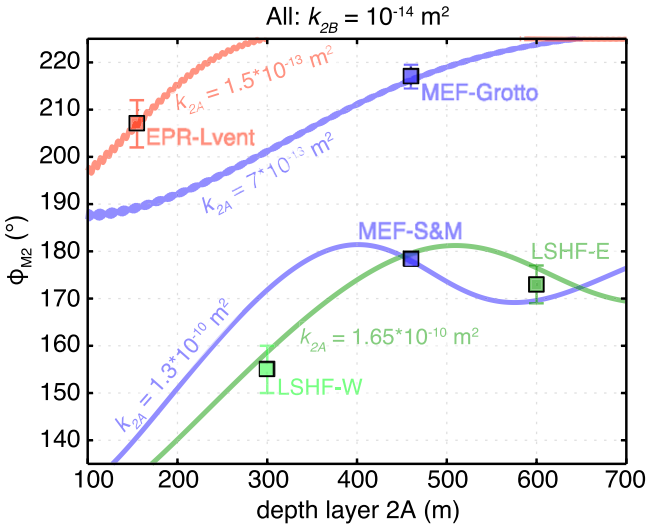

Figure 5. Effect of layer 2A thickness on the M2 phase lag, assuming a permeability of 10^{-14} m^2 in layer 2B and a range of permeabilities for layer 2A. Squares indicate measured values. See section 4.2 for details.

On the other hand, intermediate behaviors are observed at the MEF where the extrusive layer thickness is ∼450 m (Van Ark et al., 2007). Since the seismic data indicate the extrusive layer thickness is the same for both of these vents (Van Ark et al., 2007), at the MEF the phase lag difference between the two sites appears to result from a variation in layer 2A permeability rather than layer 2A thickness. Magnetic data suggest that the S&M and Grotto vents, which are separated by a distance of ∼150 m, are fed by distinct fluid upwelling zones (Tivey & Johnson, 2002), and our results suggest these zones have different layer 2A permeabilities.

5. Discussion

5.1. Preamble: Limitations of the 1-D Poroelastic Modulation Model

Our multilayer poroelastic model makes several key assumptions that we briefly review. Firstly, the 1-D formulation does not account for horizontal gradients in fluid pressure, matrix displacement, or matrix

properties, which precludes any tidally induced horizontal flow. Secondly, the use of a multilayer model with uniform permeability for each layer does not fully account for the progressive decrease in permeability with depth (e.g., cracks progressively closing with increasing depth, Carlson, 2014) nor heterogeneities. Thirdly, the model assumes that the hydrothermal fluid and the matrix are in thermal equilibrium at all depths. Fourthly, we assume that the steady state temperature gradient Γ results from adiabatic cooling alone (because of depressurization on ascent—i.e., without any heat exchange between the upwelling zone and adjacent rocks), because lateral conductive heat loss cannot be incorporated into a 1-D model, and vertical conductive heat loss is negligible in a thermal plume (Phillips, 1991). Finally, we assume that the properties of the interstitial fluid are those of pure (liquid) water. These last three assumptions preclude a discussion of how the temperature distribution inside a real convection cell might complicate the flow.

The first two assumptions dealing with spatial homogeneity are common to most permeability estimates and models, even though the matrix hosting hydrothermal circulation at MORs is fractured, faulted, fissured, and brecciated to high degrees (e.g., Escartín et al., 2007; Wright et al., 2002), which can impart significant heterogeneity to the permeability structure. To this point, most models, including that employed here, address this issue by considering length scales much larger than the heterogeneity scale, which allows the system to be characterized by an effective permeability that implicitly averages heterogeneities. Incorporating heterogeneous permeability fields into flow models is complex, computationally expensive, and more importantly, ad hoc, lacking in situ reliable constraints (particularly at depth). On the other hand, incorporating multiple layers into poroelastic flow models is more straightforward. The third assumption regarding thermal equilibrium is necessary, because we are using exit-fluid temperature fluctuations (as opposed to velocity fluctuations, for example) to constrain permeability (Jupp & Schultz, 2004) and is justified by the fact that the thermal diffusion length scale over a tidal cycle ($\sim$16 cm @ M2 and $\sim$20 cm @ K1) is less than the spacing of flow paths (i.e., faults and cracks) (e.g., Bohnenstiehl & Carbotte, 2001; Wright et al., 2002). The fourth assumption is valid in situations where there is little-to-no heat exchange between upwelling fluids and the surrounding matrix, which appears to be a valid assumption for the hydrothermal fields discussed in this study based on exit-fluid chemistry (e.g., Langmuir et al., 1997; Pester et al., 2012). The last assumption regarding fluid properties is justified as long as there are no phase changes in the tidally pumped flow regime because the fluid dynamic properties of hydrothermal fluids are similar to those of pure water.

5.2. Measured Range of Layers 2A and 2B Permeability and Comparison With Previous Work

Hydrothermal systems exhibiting phase lags between tidal loading and exit-fluid temperature greater than $\sim$200° are generally well explained by a poroelastic model in which the shallow (extrusive) crust has a moderate permeability ($k_{2A} \sim 10^{-13}$ – 10^{-12} m^2). By contrast, systems with phase lags $\leq$180° require a higher layer 2A permeability ($k_{2A} \geq 10^{-10}$ m^2). The dichotomy observed in layer 2A arises from the sensitivity of phase lag to extrusive layer permeability (Figures 2c and 2d), and suggests that phase lag constitutes a first-order proxy for the permeability of the shallowest portion of the upflow zone underlying a given hydrothermal site. This is consistent with the results of Barreyre and Sohn (2016).

High permeability in the shallow crust ($\geq 10^{-10}$ m^2)—as we infer beneath Lucky Strike and the S&M site of the MEF—has previously been proposed for the Endeavour segment near the Raven field $\sim$1 km north of the MEF through a quantitative analysis of seafloor fissuring (Hearn et al., 2013). Such high permeabilities are similar to those measured through borehole flow calculations in shallow subaerial Hawaiian basalts (10^{-11}–10^{-9} m^2) (Ingebritsen & Scholl, 1993), and upper igneous oceanic crustal units (Becker & Davis, 2004, and references therein). They are similar to in situ permeability measurements in shallow submarine wellbores (yielding values as large as 10^{-11} m^2) (Fisher, 1998), and in wellbores from sedimented ridge flanks of both the MAR and the JdFR ($\sim 10^{-10}$ m^2) (Davis et al., 2000). Permeabilities inferred from pressure diffusion along borehole transects of CORKs (i.e., Circulation Obviation Retrofit Kits) yield similarly high values (10^{-10}–10^{-9} m^2) (Davis et al., 2001), and so do large-scale numerical models of fluid flow and heat transport (10^{-11}–10^{-9} m^2) (e.g., Stein & Fisher, 2003), and ophiolite studies (10^{-12}–10^{-8} m^2, Nehlig & Juteau, 1988; Van Everdingen, 1995).

Interestingly, our model predicts lower 2A permeability beneath the Grotto site ($\sim 10^{-12}$ m^2), located between S&M and Raven. This suggests that layer 2A permeability can vary substantially from one discharge zone to the next, even zones separated by less than a km. Our model also predicts lower permeability

($\sim 10^{-13}$ m^2) in layer 2A beneath EPR's L-vent (9°46′N), which is in agreement with the $10^{-13.2}$ m^2 estimated by Marjanović et al. (2017) from seismic velocities and porosity/permeability relationships (Carlson, 2014). This contrasts with the high permeability values ($\sim 10^{-10}$–10^{-9} m^2) proposed by Crone et al. (2011) for the upflow zone beneath the 9°50′N cluster of vents located ~10 km north of L-vent. This estimate was obtained by assuming that the timing of microearthquakes directly reflects the diffusion of poroelastic stresses related to tidal cycles. This approach yielded a "background" permeability of the crust close to 10^{-12} m^2, and locally as low as 10^{-14} m^2. Significantly higher permeability ($\sim 10^{-10}$–10^{-9} m^2) was found within narrow areas of hydrothermal upflow and downflow, which highlighted the high lateral heterogeneity of the crust on length scales < 3 km. This model, however, as the one used by Marjanović et al. (2017) did not make a distinction between layers 2A and 2B permeability.

The more moderate permeability values in the 10^{-13}–10^{-12} m^2 range, which we propose for layer 2A beneath the L-vent (EPR) and Grotto (MEF) sites are consistent with estimates of 3×10^{-13}–6×10^{-12} m^2 derived by modeling flow rate perturbations generated by earthquake swarms near the MEF (Crone et al., 2010). They also fall within the range determined through drill-string packer experiments at the eastern flank of the JdFR (3×10^{-14}–2×10^{-11} m^2; Becker and Fisher, 2000).

Our two-layer model places less stringent constraints on layer 2B permeability, but does provide reliable upper bounds that increase with decreasing spreading rate: $\sim 2 \times 10^{-14}$, $\sim 10^{-13}$, and $\sim 10^{-12}$ m^2 at L-vent (EPR), MEF, and Lucky Strike, respectively (Figure 4). These lower values are closer to (but generally slightly lower than) the estimates of Lowell et al. (2013) who used a simple single-pass convection model to infer the effective, depth-averaged permeability of discharge zones based on heat flow estimates at hydrothermal sites. This suggests that the effective permeability that sets the pace of heat extraction represents some average of layers 2A and 2B permeability that is primarily influenced by layer 2B (Rosenberg et al., 1993). We further explore this notion in the following section. It should of course be noted that all the above permeability estimates, including ours, were derived by fitting a model to an observable (e.g., phase lag, heat flow, earthquake distribution). The accuracy of these estimates largely relies on the model applicability and accuracy.

5.3. Reconciling Permeability Estimates From Tidal Modulation With the Heat Output of Hydrothermal Fields

By definition, permeability sets the Darcy velocity of hydrothermal fluids subjected to a given pressure gradient (equation (11)). Permeability thus exerts a very strong modulation on the thermo-chemical fluxes associated with hydrothermal circulation (Lowell & Germanovich, 2004), as well as on venting temperature (Driesner, 2010). Here we explore the possibility of further constraining layers 2A and 2B permeability by constructing a model that jointly accounts for (1) the tidal response of hydrothermal systems, (2) their steady-state heat flow, and (3) the associated venting temperatures. We adapt the theoretical framework developed by Driesner (2010) to calculate the heat flow that would be transported by upwelling fluids in a stratified hydrothermal discharge zone of known k_{2A} and k_{2B}. In our conceptual model, buoyant upflow is fueled by an imposed heat flux resulting from the accretion of hot, crystallizing crust, and leads to venting of a total flux Q at the seafloor. In low-permeability layer 2B, the upflow is assumed to occur within a cylindrical zone of radius R_{2B}. In layer 2A, the upflow is likely faster and thus occupies a narrower area (radius R_{2A}) (Rosenberg et al., 1993). Under the assumption of steady-state heat transfer, the heat flow through layer 2A (q_{2A}, in W m^{-2}) and 2B (q_{2B}) must match the venting flux ($Q = \pi R_{2A}^2\ q_{2A} = \pi R_{2B}^2\ q_{2B}$). We write T_H and P_H the temperature and pressure of fluids at the base of layer 2B, and assume that the properties of fluids upwelling throughout layer 2B are well described by that of seawater at (T_H, P_H). Likewise, we assume that the temperature ($T^* \leq T_H$) and pressure ($P^* \leq P_H$) that characterize the interface between layers 2B and 2A provide a reasonable approximation of the properties of fluids throughout layer 2A, and that T^* can be considered a reasonable proxy for the seafloor venting temperature.

The temperature difference driving the flow through layer 2A is that between the hot fluid at temperature T^* and the ocean (T_C, at seafloor pressure P_C). The heat flow through layer 2A thus writes:

$$q_{2A} = \frac{k_{2A} g (\rho_C - \rho_*)}{\mu_*} \rho_* (h_* - h_C), \tag{20}$$

where μ is the dynamic viscosity of the fluid, ρ is its density, and h is its enthalpy (in J·kg^{-1}). Likewise, the heat flow through layer 2B is

$$q_{2B} = \frac{k_{2B} g(\rho_* - \rho_H)}{\mu_H} \rho_H (h_H - h_C). \quad (21)$$

In equations (20) and (21), subscripts "H", "*", and "C" refer to pressure-temperature conditions (P_H, T_H), (P^*, T^*), and (P_C, T_C).

For simplicity, we assume that T_H is known, and for a given Q solve equations (20) and (21) to obtain combinations of k_{2A} and k_{2B} that satisfy $Q = \pi R_{2A}^2 q_{2A} = \pi R_{2B}^2 q_{2B}$. Each ($k_{2A}$, k_{2B}) pair is associated with a unique value of T^* in the region of parameter space considered. This procedure is carried out using the tabulated thermodynamic properties of pure water and steam (IAPWS-IF97, Wagner et al., 2000), which constitute a reasonable approximation for hydrothermal fluid properties. Viscosity is estimated based on the tables of International Association for the Properties of Water and Steam (2003; *Revised release on the IAPS formulation 1985 for the viscosity of ordinary water substance*). Seafloor conditions are taken as $T_C = 4$°C and $P_C = 230$ bar. P^* and P_H are chosen as 244 and 299 bar, respectively, but their exact value has little influence on the result compared to the choice of T_H. We choose $T_H = 450$°C but recognize that any value between 420 and 600°C would be equally acceptable as modeling studies have shown that this range of basal temperatures is compatible with observed seafloor venting temperatures (Fontaine & Wilcock, 2007; Fontaine et al., 2001). Finally, to simplify our exploration of a vast parameter space, we consider two cases with $R_{2B} = 500$ and 100 m, and assume $R_{2A} = R_{2B}/10$.

Using this relatively simple model, we constrain combinations of k_{2A} and k_{2B} that are consistent with three values of Q which we consider representative of EPR's L-vent (160 MW), MEF (450 MW), and Lucky Strike (600 MW) (Lowell et al., 2013 and references therein). Of course, these estimates have large error bars, potentially larger than ±50%. Further, we must use the estimated heat output of the EPR 9°50′N hydrothermal field as a proxy for heat flow in the neighboring L-vent area, as no estimate of the heat output of that region is currently available. The exercise attempted here should therefore be considered as a proof-of-concept for a methodology that reconciles the permeability constraints of tidal modulation, steady-state heat transfer and venting temperature. It is however useful in this context to compare the characteristics of various hydrothermal sites in a quantitative fashion.

Figure 6 shows two sets of curves indicating which permeability combinations can explain the observed heat outputs under two distinct assumptions for the radius of the cylindrical upflow zone in layer 2B: $R_{2B} = 500$ and 100 m. Focusing first on the $R_{2B} = 500$ m case, which is consistent with the structure of upflow zones inferred from microseismicity studies at EPR 9°50′N (Marjanović et al., 2017; Tolstoy et al., 2008), it is apparent that heat flow is primarily sensitive to the permeability of layer 2B, which is consistent with earlier studies (e.g., Rosenberg et al., 1993). Further, this permeability is likely greater than 10^{-15} m^2 as a lower value would not permit the observed heat fluxes. At L-vent, a permeability of 6×10^{-15} m^2 in layer 2B and 2×10^{-13} m^2 in layer 2A (red star in Figure 6) would enable a heat flow of 160 MW over a 50 m radius upwelling zone in layer 2A, while also producing the observed phase lag between tidal loading and vent temperature. Interestingly, a much higher permeability ($\sim 10^{-10}$ m^2) as suggested by Crone et al. (2011) throughout the crust beneath EPR 9°50′N would likely result in unrealistically high heat flow and potentially lower temperature discharge (Driesner, 2010). More targeted studies of the fine permeability structure of EPR will be required to assess the applicability, sensitivity, and potential biases of each approach.

Similarly, $k_{2B} = 10^{-14}$ m^2 and $k_{2A} = 7 \times 10^{-13}$ m^2 would be a plausible combination for the Grotto site of the MEF. Our model is in both cases compatible with a shallow upwelling temperature in excess of 300°C, which is consistent with high-temperature venting occurring at both sites. By contrast, models satisfying heat flow and tidal modulation constraints at S&M and Lucky Strike require much greater layer 2A permeability (on the order of 10^{-10} m^2), and layer 2B permeabilities similar to those inferred beneath L-vent and Grotto (between 10^{-14} and 10^{-15} m^2). However, such models would predict moderate-to-low venting temperatures (<150°C) instead of the high temperatures observed at these sites. Alternatively, one can assume a narrower upwelling zone throughout the crust ($R_{2B} = 100$ m), in which case models can jointly explain the phase lag, heat output and venting temperatures in excess of 200°C with higher k_{2B} values ($\sim 2 \times 10^{-13}$ m^2, blue and green stars in Figure 6).

Large uncertainties on T_H, Q, and the size of crustal-scale upflow zones preclude any definitive estimate of k_{2A} and k_{2B} at the hydrothermal sites considered. However, the methodology outlined here could be applied at a more local scale beneath a particular venting site, where permeability layering could be better constrained. In the context of our study, this method provides useful guidelines to evaluate the plausibility of our permeability estimates. The most important one is that layer 2B permeability is likely greater than $\sim 10^{-15}$ m^2. This lower bound common to all sites provides a reasonably narrow range of permeability for

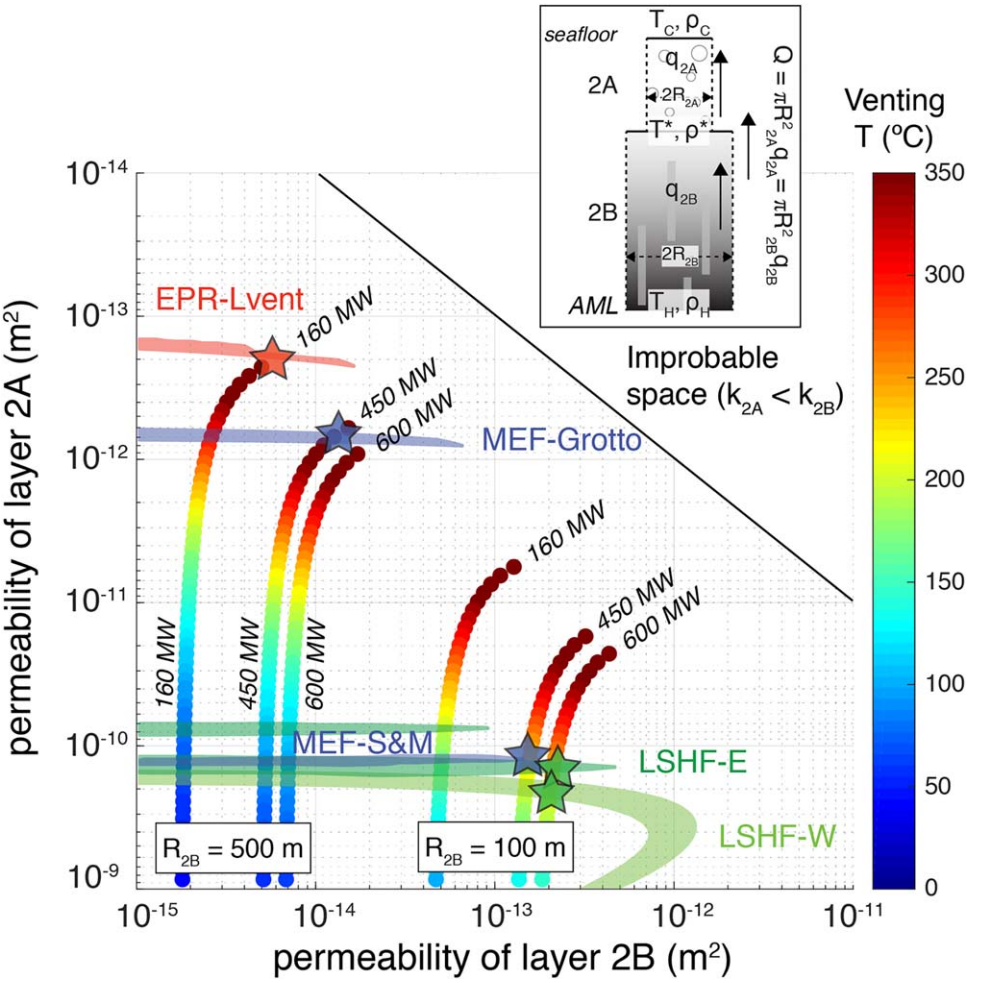

Figure 6. Joint constraints on layers 2A and 2B permeability. Colored areas mark possible combinations of k_{2A} and k_{2B} compatible with the observed phase lag between tidal loading and vent temperatures. Colored lines indicate combinations of k_{2A} and k_{2B} compatible with a heat flow of 160, 450, or 600 MW in a cylindrical upflow zone of radius R_{2B} *and* R_{2A}, under the model assumptions presented in section 5.3. Two cases are shown—i.e., for $R_{2B} = 500$ and 100 m. Lines are color-coded by the associated venting temperature T^*. Colored stars indicate possible combinations of k_{2A} and k_{2B} that jointly satisfy constraints from tidal modulation and heat flow.

layer 2B beneath L-vent at the EPR: $10^{-15} - 2 \times 10^{-14}$ m^2. Figure 6 shows that layer 2B permeability could fall within that same low range at all other sites and satisfy the heat flow constraint. In that scenario, the variability in permeability structure from site to site—and potentially across spreading rates—would be primarily confined to layer 2A, with moderate-to-low k_{2A} at the fast-spreading EPR, both high and low k_{2A} in neighboring upflow zones on the intermediate-spreading JdFR, and high k_{2A} at the slow-spreading MAR. However, as the model also shows, high 2A permeabilities are difficult to reconcile with high-temperature venting (Driesner, 2010), unless upwelling zones are relatively focused (radius $\leq$ 100 m). If that were the case, greater 2B permeability ($\sim 10^{-13}$ m^2) could enable greater venting temperatures at the intermediate and slow-spreading sites, and a greater Rayleigh number characterizing the convection system, which would be consistent with narrower upflow zones (Fontaine & Wilcock, 2007; Lowell & Germanovich, 2004). In that alternate scenario, both layers 2A and 2B permeability would increase with decreasing spreading rate.

An increase in upflow zone permeability at slower spreading rates is broadly consistent with the tectonomagmatic conditions that prevail in such settings, especially with regards to layer 2A. Along slow-spreading MORs (e.g., at the LSHF), the upper crust and its extrusive portion (i.e., layer 2A) are relatively thick (Cannat, 1996; Hooft et al., 2000; Hussenoeder et al., 2002; Smith & Cann, 1993) and tectonized by faults and fissures that accommodate a large fraction (>0.5) of plate separation (Behn & Ito, 2008; Buck et al., 2005). A greater

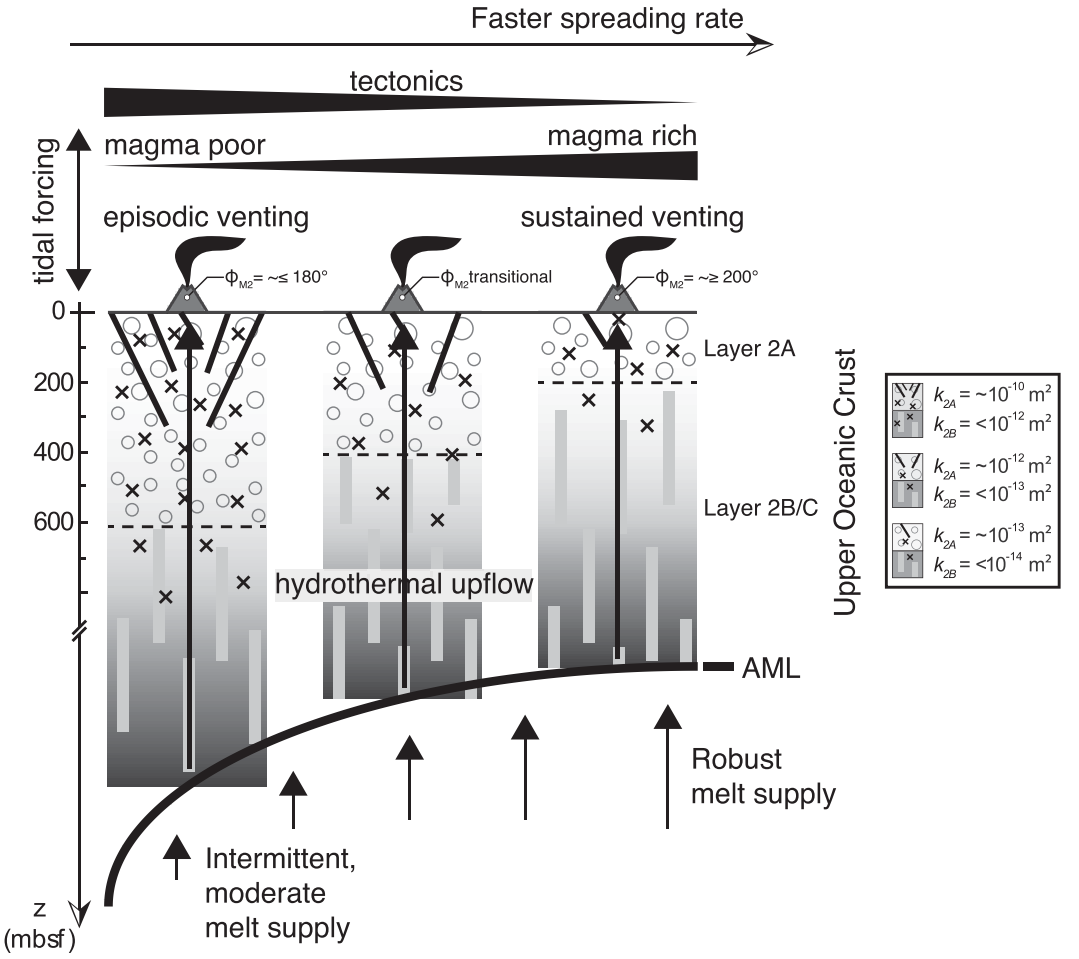

Figure 7. A conceptual model for changes in permeability layering and effective heat output in basalt-hosted systems across ridge spreading rates. Schematic cross sections represent typical upper oceanic crust stratification with corresponding permeabilities. In this interpretation, the variability in layer 2A upflow zone permeability across spreading rates primarily reflects the pervasiveness of tectonic processes in the shallow extrusive layer.

degree of faulting likely results in more widespread damage zones, which increases the matrix permeability. By contrast, at fast-spreading ridges (e.g., the EPR), magmatic processes accommodate a greater fraction of plate spreading (Behn & Ito, 2008; Buck et al., 2005; Cowie et al., 1993), resulting in a thinner, less tectonized upper crust and a layer 2A that is frequently repaved by lava flows (e.g., Fornari et al., 2004, 2012). Robust magmatism at fast-spreading ridges thus hinders the formation of high-permeability upflow zones, potentially providing a simple explanation for the differences in phase lag and permeability structure observed between the LSHF and the EPR vent fields. This simple conceptual framework is illustrated in Figure 7.

It is of course difficult to infer general trends in permeability layering versus spreading rate with the limited data set at our disposal. This is particularly true given that our estimates for the JdFR suggest considerable variability in upflow zone permeability between neighboring upflow zones. Such short-wavelength ($<$ 1 km) heterogeneity is unlikely to reflect changes in tectono-magmatic conditions, and may instead relate to hydrothermal alteration and mineralization processes active on a local scale. In any case, applying the methodology presented in this study to many other sites along the global MOR system will provide meaningful constraints on the natural variability of upflow zone permeability and its possible correlation with spreading rate.

6. Conclusions

We have developed an analytical multilayer poroelastic model and applied it to a comprehensive data set of in situ exit-fluid temperature time series data from sites where the phase lag between these data and

ocean tidal loading can be robustly constrained, and the first-order crustal layering is well-constrained by seismic data. Applying our model to these data allows us to constrain the depth-dependent permeability structure of upflow zones across MOR hydrothermal fields. Our main conclusions are as follows:

1. Overall, we model the shallow crust beneath vents with phase lags $\geq 200°$ as a low-permeability $\left(k_{2A} \sim 10^{-13}-10^{-12}\ \mathrm{m}^2\right)$ extrusive layer 2A, and the shallow crust beneath vents with phase lags $\leq 180°$ as a relatively high-permeability $\left(k_{2A} \sim \geq\ 10^{-10}\ \mathrm{m}^2\right)$ extrusive layer 2A.
2. Our model and methodology places less stringent constraints on deeper crust (i.e., layer 2B) permeability, but does provide reliable upper bounds: $\sim 10^{-14}$, $\sim 10^{-13}$, and $\sim 10^{-12}$ m^2 at L-vent (EPR), MEF, and Lucky Strike, respectively, and plausible lower bound of $\sim 10^{-15}$ m^2 to satisfy heat flow constraints.
3. Our results are compatible with a scenario in which both layers 2A and 2B upflow zone permeability increase with decreasing spreading rate. This is consistent with the tectono-magmatic conditions that characterize different spreading rates (i.e., a greater degree of faulting at slow-spreading MORs increasing matrix permeability, and a greater degree of magmatism at fast-spreading MORs likely resulting in a less tectonized crust that is frequently repaved by lava flows.)

Appendix A: Synthesis of Relevant Poroelastic Parameters

Here, we list the equations used to estimate the properties of the hydrothermal fluid and oceanic crust (elastic matrix):

1. Bulk density: $\rho = \phi\rho_f + (1-\phi)\rho_s$.
2. Shear modulus: $G = \rho V_S^2$.
3. Matrix drained bulk modulus: $K = \dfrac{G\left[\frac{4}{3} - \frac{V_P^2}{V_S^2}\right]\left[\frac{\phi}{K_f} + \frac{1-\phi}{K_s}\right] + 1}{\frac{G}{K_s^2}\left[\frac{4}{3} - \frac{V_P^2}{V_S^2}\right] - \left[\frac{\phi}{K_f} - \frac{1+\phi}{K_s}\right]}$.
4. Fluid bulk modulus: $K_f = \rho_f \frac{\partial P}{\partial \rho_f}\Big|_{H=cst}$, H is specific enthalpy and P is the steady state pore pressure (Pa).
5. Dimensionless poroelastic stress coefficient (Detournay & Cheng, 1993): $\psi = \frac{\alpha(1-2\nu)}{2(1-\nu)}$.
6. Drained Poisson's ratio of the matrix frame: $\nu = \frac{3K-2G}{2(3K+G)}$.
7. Biot-Willis parameter—coefficient of effective stress—defined as a measure of the relative magnitude of the matrix and grain bulk moduli (Nur & Byerlee, 1971): $\alpha = 1 - \frac{K}{K_s}$.
8. Skempton's coefficient: $\beta = \alpha\left[\alpha + \phi K\left(\frac{1}{K_f} - \frac{1}{K_s}\right)\right]^{-1}$.

Acknowledgments
This research was funded by the National Science Foundation grants (OCE-1536705 & OCE-1536943) and postdoctoral scholarships from Woods Hole Oceanographic Institution and Lamont-Doherty Earth Observatory. Data used in this study can be found at Marine Geoscience Data System (MGDS—http://www.marine-geo.org/index.php), PANGAEA (http://doi.pangaea.de/10.1594/PANGAEA.820343), European Multidisciplinary Seafloor and water column Observatory (EMSO—http://www.emso-fr.org/), and Ocean Networks Canada (ONC—http://dmas.uvic.ca/DataSearch). The authors are grateful to William Wilcock and Lars Rüpke for detailed and constructive reviews that significantly improved the manuscript and to Editor Joshua Feinberg. Finally, I dedicate this paper to B.T. and A.T.B.

References

Arnulf, A. F., Singh, S. C., Harding, A. J., Kent, G. M., & Crawford, W. (2011). Strong seismic heterogeneity in layer 2A near hydrothermal vents at the Mid-Atlantic Ridge. *Geophysical Research Letters*, *38*, L13320. https://doi.org/10.1029/2011GL047753

Barreyre, T., Escartín, J., Garcia, R., Cannat, M., Mittelstaedt, E., & Prados, R. (2012). Structure, temporal evolution, and heat flux estimates from the Lucky Strike deep-sea hydrothermal field derived from seafloor image mosaics. *Geochemistry, Geophysics, Geosystems*, *13*, Q04007. https://doi.org/10.1029/2011GC003990

Barreyre, T., Escartín, J., Sohn, R., & Cannat, M. (2014a). Permeability of the Lucky Strike deep-sea hydrothermal system: Constraints from the poroelastic response to ocean tidal loading. *Earth and Planetary Science Letters*, *408*, 146–154.

Barreyre, T., Escartín, J., Sohn, R., Cannat, M., Ballu, V., & Crawford, W. (2014b). Temporal variability and tidal modulation of hydrothermal exit-fluid temperatures at the Lucky Strike deep-sea vent field, Mid-Atlantic Ridge. *Journal of Geophysical Research: Solid Earth*, *119*, 2543–2566. https://doi.org/10.1002/2013JB010478

Barreyre, T., & Sohn, R. A. (2016). Poroelastic response of mid-ocean ridge hydrothermal systems to ocean tidal loading: Implications for shallow permeability structure. *Geophysical Research Letters*, *43*, 1660–1668. https://doi.org/10.1002/2015GL066479

Becker, K. (1985). Large-scale electrical resistivity and bulk porosity of the oceanic crust, Deep Sea Drilling Project Hole 504B. Costa Rica Rift. *Initial Report Deep Sea Drilling Project*, *83*, 419–427. https://doi.org/10.2973/dsdp.proc.83.1985

Becker, K., & Davis, E. E. (2003). New evidence for age variation and scale effects of permeabilities of young oceanic crust from borehole thermal and pressure measurements. *Earth and Planetary Science Letters*, *210*, 499–508.

Becker, K., & Davis, E. E. (2004). In situ determinations of the permeability of the igneous oceanic crust. In E. E. Davis & H. Elderfield (Eds.), *Hydrogeology of the oceanic lithosphere* (pp. 189–224). Cambridge, UK: Cambridge University Press.

Becker, K., & Fisher, A. T. (2000). Permeability of upper oceanic basement on the eastern flank of the Juan de Fuca Ridge determined with drill-string packer experiments. *Journal of Geophysical Research*, *105*(B1), 897–912. https://doi.org/10.1029/1999JB900250

Becker, K., & Fisher, A. T. (2008). Borehole packer tests at multiple depths resolve distinct hydrologic intervals in 3.5-Ma upper oceanic crust on the eastern flank of Juan de Fuca Ridge. *Journal of Geophysical Research*, *113*, B07105. https://doi.org/10.1029/2007JB005446

Behn, M. D., & Ito, G. (2008). Magmatic and tectonic extension at mid-ocean ridges: 1. Controls on fault characteristics. *Geochemistry, Geophysics, Geosystems*, *9*, Q08O10. https://doi.org/10.1029/2008GC001965

Biot, M. A. (1941). General theory of three-dimensional consolidation. *Journal of Applied Physics*, *12*, 155–164.
Bohnenstiehl, D. R., & Carbotte, S. M. (2001). Faulting patterns near 19°30′ S on the East Pacific rise: Fault formation and growth at a superfast spreading center. *Geochemistry, Geophysics, Geosystems*, *2*(9), 1056. https://doi.org/10.1029/2001GC000156
Buck, W. R., Lavier, L. L., & Poliakov, A. N. (2005). Modes of faulting at mid-ocean ridges. *Nature*, *434*(7034), 719–723.
Cann, J. R., & Strens, M. R. (1989). Modeling periodic megaplume emission by black smoker systems. *Journal of Geophysical Research*, *94*(B9), 12227–12237. https://doi.org/10.1029/JB094iB09p12227
Cannat, M. (1996). How thick is the magmatic crust at slow-spreading oceanic ridges? *Journal of Geophysical Research*, *101*(B2), 2847–2857. https://doi.org/10.1029/95JB03116
Cannat, M. (1999). Mid-Atlantic Ridge-Azores hotspot interactions: Along-axis migration of a hotspot-derived magmatic pulse 14 to 4 ma ago. *Earth and Planetary Science Letters*, *173*, 257–269.
Carbotte, S. M., & Macdonald, K. C. (1994). Comparison of sea floor tectonic fabric created at intermediate, fast and superfast spreading ridges: Influence of spreading rate, plate motions, and ridge segmentation on fault patterns. *Journal of Geophysical Research*, *99*(B7), 13609–13633. https://doi.org/10.1029/93JB02971
Carlson, R. L. (2014). The influence of porosity and crack morphology on seismic velocity and permeability in the upper oceanic crust. *Geochemistry, Geophysics, Geosystems*, *15*, 10–27. https://doi.org/10.1002/2013GC004965
Carmichael, R. S. (1966). *Handbook of physical properties of rocks, II* (345 p.). Boca Raton, FL: CRC Press.
Christensen, N. I., & Salisbury, M. H. (1972). Sea floor spreading, progressive alteration of layer 2 basalts, and associated changes in seismic velocities. *Earth and Planetary Science Letters*, *15*, 367–375.
Christeson, G. L., Kent, G. M., Purdy, G. M., & Detrick, R. S. (1996). Extrusive thickness variability at the East Pacific Rise, 9°–10°N: Constraints from seismic techniques. *Journal of Geophysical Research*, *101*(B2), 2859–2873. https://doi.org/10.1029/95JB03212
Coumou, D., Driesner, T., & Heinrich, C. A. (2008). The structure and dynamics of mid-ocean ridge hydrothermal systems. *Science*, *321*(5897), 1825–1828.
Cowie, P. A., Scholz, C. H., Edwards, M., & Malinverno, A. (1993). Fault strain and seismic coupling on mid-ocean ridges. *Journal of Geophysical Research*, *98*(B10), 17911–17920. https://doi.org/10.1029/93JB01567
Crawford, W. C., Rai, A., Singh, S. C., Cannat, M., Escartín, J., Wang, H., et al. (2013). Hydrothermal seismicity beneath the summit of Lucky Strike volcano, Mid-Atlantic Ridge. *Earth and Planetary Science Letters*, *373*, 118–128. https://doi.org/10.1016/j.epsl.2013.04.028i
Crone, T. J., Tolstoy, M., & Stroup, D. F. (2011). Permeability structure of young ocean crust from poroelastically triggered earthquakes. *Geophysical Research Letters*, *38*, L05305. https://doi.org/10.1029/2011GL046820
Crone, T. J., & Wilcock, S. D. (2005). Modeling the effects of tidal loading on mid-ocean ridge hydrothermal systems. *Geochemistry, Geophysics, Geosystems*, *6*, Q07001. https://doi.org/10.1029/2004GC000905
Crone, T. J., Wilcock, W. S. D., & McDuff, R. E. (2010). Flow rate perturbations in a black smoker hydrothermal vent in response to a mid-ocean ridge earthquake swarm. *Geochemistry, Geophysics, Geosystems*, *11*, Q03012. https://doi.org/10.1029/2009GC002926
Davis, E. E., LaBonte, A., He, J., Becker, K., & Fisher, A. (2010). Thermally stimulated "runaway" downhole flow in a superhydrostatic ocean crustal borehole: Observations, simulations, and inferences regarding crustal permeability. *Journal of Geophysical Research*, *115*, B07102. https://doi.org/10.1029/2009JB006986
Davis, E. E., Wang, K., Becker, K., & Thomson, R. E. (2000). Formation-scale hydraulic and mechanical properties of oceanic crust inferred from pore pressure response to periodic seafloor loading. *Journal of Geophysical Research*, *105*(B6), 13423–13435. https://doi.org/10.1029/2000JB900084
Davis, E. E., Wang, K., Thomson, R. E., Becker, K., & Cassidy, J. F. (2001). An episode of seafloor spreading and associated plate deformation inferred from crustal fluid pressure transients. *Journal of Geophysical Research*, *106*(B10), 21953–21963. https://doi.org/10.1029/2000JB000040
Detournay, E., & Cheng, A. H.-D. (1993). Fundamentals of poroelasticity. In J. A. Hudson & C. Fairhurst (Eds.), *Comprehensive rock engineering: Principles, practice and projects* (Vol. 2, pp. 113–171). New York, NY: Elsevier.
Detrick, R. S., Buhl, P., Vera, E., Mutter, J., Orcutt, J., Madsen, J., et al. (1987). Multi-channel seismic imaging of a crustal magma chamber along the East Pacific rise. *Nature*, *326*(6108), 35–41.
Driesner, T. (2010). The interplay of permeability and fluid properties as a first order control of heat transport, venting temperatures and venting salinities at mid-ocean ridge hydrothermal systems. *Geofluids*, *10*(1–2), 132–141.
Edmond, J. M., Measures, C., McDuff, R. E., Chan, L. H., Collier, R., Grant, B., et al. (1979). Ridge crest hydrothermal activity and the balances of the major and minor elements in the ocean: The Galapagos data. *Earth and Planetary Science Letters*, *46*(1), 1–18. https://doi.org/10.1016/0012-821X(79)90061-X
Elderfield, H., & Schultz, A. (1996). Mid-ocean ridge hydrothermal fluxes and the chemical composition of the ocean. *Annual Reviews of Earth and Planetary Sciences*, *24*(1), 191–224.
Emmanuel, S., & Berkowitz, B. (2006). Suppression and stimulation of seafloor hydrothermal convection by exothermic mineral hydration. *Earth and Planetary Science Letters*, *243*(3–4), 657–668.
Escartín, J., Soule, S. A., Fornari, D. J., Tivey, M. A., Schouten, H., & Perfit, M. R. (2007). Interplay between faults and lava flows in construction of the upper oceanic crust: The East Pacific Rise crest 9°25′–9°58′ N. *Geochemistry, Geophysics, Geosystems*, *8*, Q06005. https://doi.org/10.1029/2006GC001399
Fisher, A. T. (1998). Permeability within basaltic oceanic crust. *Reviews of Geophysics*, *36*(2), 143–182. https://doi.org/10.1029/97RG02916
Fisher, A. T. (2004). Rates and patterns of fluid circulation. In E. E. Davis and H. Elderfield, *Hydrogeology of the oceanic lithosphere* (pp. 339–377). Cambridge, UK: Cambridge University Press.
Fisher, A. T., Davis, E. E., & Becker, K. (2008). Borehole-to-borehole hydrologic response across 2.4 km in the upper oceanic crust: Implications for crustal-scale properties. *Journal of Geophysical Research*, *113*, B07106. https://doi.org/10.1029/2007JB005447
Fontaine, F. J., Rabinowicz, M., & Boulègue, J. (2001). Permeability changes due to mineral diagenesis in fractured crust: Implications for hydrothermal circulation at mid-ocean ridges. *Earth and Planetary Science Letters*, *184*, 407–425.
Fontaine, F. J., & Wilcock, W. S. D. (2007). Two-dimensional numerical models on open-top hydrothermal convection on high Rayleigh and Nusselt numbers: Implications for mid-ocean ridge hydrothermal circulation. *Geochemistry, Geophysics, Geosystems*, *8*, Q07010. https://doi.org/10.1029/2007GC001601
Fontaine, F. J., Wilcock, W. S. D., & Butterfield, D. A. (2007). Physical controls on the salinity of mid-ocean ridge hydrothermal fields. *Earth and Planetary Science Letters*, *257*(1–2), 132–145.
Fornari, D. J. (2004). Submarine lava flow emplacement at the East Pacific Rise 9°50′N: Implications for uppermost ocean crust stratigraphy and hydrothermal fluid circulation. In C. R. German, et al. (Eds.), *Mid-ocean ridges: Hydrothermal interactions between the lithosphere and oceans*, *Geophysical Monograph Series* (Vol. 148, pp. 187–218). Washington, DC: American Geophysical Union.

Fornari, D. J., Shank, T., Von Damm, K. L., Gregg, T. K. P., Lilley, M., Levai, G., et al. (1998). Time-series temperature measurements at high-temperature hydrothermal vents, East Pacific Rise 9°49′–51′N: Evidence for monitoring a crustal cracking event. *Earth and Planetary Science Letters*, *160*(3–4), 419–431.

Fornari, D. J., Von Damm, K., Bryce, J., Cowen, J., Ferrini, V., Fundis, A., et al. (2012). The East Pacific rise between 9°N and 10°N: Twenty-five years of integrated, multidisciplinary oceanic spreading center studies. *Oceanography*, *25*(1), 18–43. https://doi.org/10.5670/oceanog.2012.02

Fouquet, Y., Ondréas, H., Charlou, J.-L., Donval, J.-P., Radford-Knoery, J., Costa, I., et al. (1995), Atlantic lava lakes and hot vents. *Nature*, *377*, 201. https://doi.org/10.1038/377201a0

Gassmann, F. (1951). Über die elastizität poröser medien. *Vierteljahrsschrift der Naturforschenden Gesellschaft in Zürich*, *96*(1), 1–23.

Germanovich, L. N., Hurt, R. S., Smith, J. E., Genc, G., & Lowell, R. P. (2015). Measuring fluid flow and heat output in seafloor hydrothermal environments. *Journal of Geophysical Research: Solid Earth*, *120*, 8031–8055. https://doi.org/10.1002/2015JB012245

Germanovich, L. N., Lowell, R. P., & Ramondenc, P. (2011). Magmatic origin of hydrothermal response to earthquake swarms: Constraints from heat flow and geochemical data. *Journal of Geophysical Research*, *116*, B05103. https://doi.org/10.1029/2009JB006588

Harding, A. J., Kent, G. M., & Orcutt, J. A. (1993). A multichannel seismic investigation of upper crustal structure at 9°N on the East Pacific Rise: Implications for crustal accretion. *Journal of Geophysical Research*, *98*(B8), 13925–13944. https://doi.org/10.1029/93JB00886

Hasenclever, J., Theissen-Krah, S., Rüpke, L. H., Morgan, J. P., Iyer, K., Petersen, S., et al. (2014). Hybrid shallow on-axis and deep off-axis hydrothermal circulation at fast-spreading ridges. *Nature*, *508*(7497), 508.

Haymon, R. M., Fornari, D. J., Von Damm, K. L., Lilley, M. D., Perfit, M. R., Edmond, J. M., et al. (1993). Volcanic eruption of the mid-ocean ridge along the East Pacific Rise crest at 9°45–52′N: Direct submersible observations of seafloor phenomena associated with an eruption event in April, 1991. *Earth and Planetary Science Letters*, *119*(1–2), 85–101.

Hearn, C. K., Homola, K. L., & Johnson, H. P. (2013). Surficial permeability of the axial valley seafloor: Endeavour Segment, Juan de Fuca Ridge. *Geochemistry, Geophysics, Geosystems*, *14*, 3409–3424. https://doi.org/10.1002/ggge.20209

Holzbecher, E. O. (1998). *Modeling density-driven flow in porous media*. New York, NY: Springer.

Hooft, E. E., Detrick, R. S., Toomey, D. R., Collins, J. A., & Lin, J. (2000). Crustal thickness and structure along three contrasting spreading segments of the Mid-Atlantic Ridge, 33.5°–35°N. *Journal of Geophysical Research*, *105*(B4), 8205–8226. https://doi.org/10.1029/1999JB900442

Humphris, S. E., Zierenberg, R. A., Mullineaux, L. S., & Thompson, R. E. (Eds.) (1995). *Seafloor hydrothermal systems: Physical, chemical, biologic and geological interactions*, *Geophysical Monograph Series* (Vol. 91, 466 p.). Washington, DC: American Geophysical Union.

Hussenoeder, S. A., Kent, G. M., & Detrick, R. S. (2002). Upper crustal seismic structure of the slow spreading Mid-Atlantic Ridge, 35 degrees N: Constraints on volcanic emplacement processes. *Journal of Geophysical Research*, *107*(B8), 2156. https://doi.org/10.1029/2001JB001691

Ingebritsen, S. E., & Scholl, M. A. (1993). The hydrogeology of Kilauea volcano. *Geothermics*, *22*, 255–270.

Jupp, T. E., & Schultz, A. (2004). A poroelastic model for the tidal modulation of seafloor hydrothermal systems. *Journal of Geophysical Research*, *109*, B03105. https://doi.org/10.1029/2003JB002583

International Association for the Properties of Water and Steam (IAPWS) (2003). *Revised release on the IAPS formulation 1985 for the viscosity of ordinary water substance*. London, UK: Author.

Iyer, K., Rüpke, L. H., & Morgan, J. P. (2010). Feedbacks between mantle hydration and hydrothermal convection at ocean spreading centers. *Earth and Planetary Science Letters*, *296*(1–2), 34–44.

Kelley, D. S., Baross, J. A., & Delaney, J. R. (2002). Volcanoes, fluids, and life at Mid-Ocean Ridge spreading centers. *Annual Review of Earth and Planetary Sciences*, *30*(1), 385–491.

Langmuir, C., Humphris, S., Fornari, D., Van Dover, C., Von Damm, K., Tivey, M. K., et al. (1997). Hydrothermal vents near a mantle hot spot: The lucky strike vent field at 37°N on the Mid-Atlantic Ridge. *Earth and Planetary Science Letters*, *148*(1–2), 69–91.

Larson, B. I., Lilley, M. D., & Olson, E. J. (2009). Parameters of subsurface brines and hydrothermal processes 12–15 months after the 1999 magmatic event at the Main Endeavor Field as inferred from in situ time series measurements of chloride and temperature. *Journal of Geophysical Research*, *114*, B01207. https://doi.org/10.1029/2008JB005627

Lilley, M. D., Butterfield, D. A., Lupton, J. E., & Olson, E. J. (2003). Magmatic events can produce rapid changes in hydrothermal vent chemistry. *Nature*, *422*(6934), 878.

Lowell, R. P., Farough, A., Hoover, J., & Cummings, K. (2013). Characteristics of magma-driven hydrothermal systems at oceanic spreading centers. *Geochemistry, Geophysics, Geosystems*, *14*, 1756–1770. https://doi.org/10.1002/ggge.20109

Lowell, R. P., & Germanovich, L. N. (2004). Hydrothermal processes at mid-ocean ridges: Results from scale analysis and single-pass models. In C. R. German (Ed.), *Mid-Ocean Ridges: Hydrothermal interactions between the lithosphere and oceans*, *Geophysical Monograph Series* (Vol. 148, pp. 219–244). Washington, DC: American Geophysical Union.

Lutz, R. A., Shank, T. M., Luther III, G. W., Vetriani, C., Tolstoy, M., Nuzzio, D. B., et al. (2008). Interrelationships between vent fluid chemistry, temperature, seismic activity, and biological community structure at a mussel-dominated, deep-sea hydrothermal vent along the East Pacific Rise. *Journal of Shellfish Research*, *27*(1), 177–190.

Luyendyk, B. P. (1984). On-bottom gravity profile across the East Pacific Rise crest at 21° north. *Geophysics*, *49*(12), 2166–2177.

Marcon, Y., Sahling, H., Borowski, C., dos Santos Ferreira, C., Thal, J., & Bohrmann, G. (2013). Megafaunal distribution and assessment of total methane and sulfide consumption by mussel beds at Menez Gwen hydrothermal vent, based on geo-referenced photomosaics. *Deep Sea Research Part I: Oceanographic Research Papers*, *75*, 93–109.

Marjanović, M., Fuji, N., Singh, S. C., Belahi, T., & Escartín, J. (2017). Seismic signatures of hydrothermal pathways along the East Pacific Rise between 9°16′ and 9°56′N. *Journal of Geophysical Research: Solid Earth*, *122*, 10241–10262. https://doi.org/10.1002/2017JB015004

Mittelstaedt, E., Davaille, A., van Keken, P. E., Gracias, N., & Escartín, J. (2010). A noninvasive method for measuring the velocity of diffuse hydrothermal flow by tracking moving refractive index anomalies. *Geochemistry, Geophysics, Geosystems*, *11*, Q10005. https://doi.org/10.1029/2010GC003227

Mittelstaedt, E., Escartín, J., Gracias, N., Olive, J.-A. L., Barreyre, T., Davaille, A., et al. (2012). Quantifying diffuse and discrete venting at the Tour Eiffel vent site, Lucky Strike hydrothermal field. *Geochemistry Geophysics Geosystems*, *13*, Q04008. https://doi.org/10.1029/2011GC003991

Mittelstaedt, E., Fornari, D. J., Crone, T. J., Kinsey, J., Kelley, D., & Elend, M. (2016). Diffuse venting at the ASHES hydrothermal field: Heat flux and tidally modulated flow variability derived from in situ time-series measurements. *Geochemistry, Geophysics, Geosystems*, *17*, 1435–1453. https://doi.org/10.1002/2015GC006144

Nees, H. A., Moore, T. S., Mullaugh, K. M., Holyoke, R. R., Janzen, C. P., Ma, S., et al. (2008). Hydrothermal vent mussel habitat chemistry, pre- and post-eruption at 9o50 North on the East Pacific Rise. *Journal of Shellfish Research*, *27*(1), 169–175.

Nehlig, P., & Juteau, T. (1988). Flow porosities, permeabilities and preliminary data on fluid inclusions and fossil thermal gradients in the crustal sequence of the Sumail ophiolite (Oman). *Tectonophysics*, *151*(1–4), 199–221.

Nur, A., & Byerlee, J. D. (1971). An exact effective stress law for elastic deformation of rock with fluids. *Journal of Geophysical Research*, *76*(26), 6414–6419. https://doi.org/10.1029/JB076i026p06414

Ondréas, H., Cannat, M., Fouquet, Y., Normand, A., Sarradin, P.-M., & Sarrazin, J. (2009). Recent volcanic events and the distribution of hydrothermal venting at the Lucky Strike hydrothermal field, Mid-Atlantic Ridge. *Geochemistry, Geophysics, Geosystems*, *10*, Q02006. https://doi.org/10.1029/2008GC002171

Percival, D., & Walden, A. (1993). *Spectral analysis for physical applications*. Cambridge, UK: Cambridge University Press.

Pester, N. J., Reeves, E. P., Rough, M. E., Ding, K., Seewald, J. S., & Seyfried, W. E. (2012). Subseafloor phase equilibria in high-temperature hydrothermal fluids of the Lucky Strike Seamount (Mid-Atlantic Ridge, 37°17′N). *Geochimica et Cosmochimica Acta*, *90*, 303–322.

Phillips, O. M. (1991). *Flow and reactions in permeable rocks*. New York, NY: Cambridge University Press.

Pros, Z., Vanek, J., & Klima, K. (1962). The velocity of elastic waves in diabase and greywacke under pressure up to 4 kilobars, Stud. *Studia Geophysica et Geodaetica*, *6*, 347–367.

Rabinowicz, M., Sempéré, J. C., & Genthon, P. (1999). Thermal convection in a vertical permeable slot: Implications for hydrothermal circulation along mid-ocean ridges. *Journal of Geophysical Research*, *104*(B12), 29275–29292. https://doi.org/10.1029/1999JB900259

Ray, R. D. (2013). Precise comparisons of bottom-pressure and altimetric ocean tides. *Journal of Geophysical Research: Oceans*, *118*, 4570–4584. https://doi.org/10.1002/jgrc.20336

Riddihough, R. (1984). Recent movements of the Juan de Fuca Plate System. *Journal of Geophysical Research*, *89*(B8), 6980–6994. https://doi.org/10.1029/JB089iB08p06980

Rosenberg, N. D., Spera, F. T., & Haymon, R. M. (1993). The relationship between flow and permeability field in seafloor hydrothermal systems. *Earth and Planetary Science Letters*, *116*(1), 135–153.

Rubin, K. H., Macdougall, J. D., & Perfit, M. R. (1994). ^{210}Po–^{210}Pb dating of recent volcanic eruptions on the sea floor. *Nature*, *368*(6474), 841–844.

Scheirer, D. S., Shank, T. M., & Fornari, D. J. (2006). Temperature variations at diffuse and focused flow hydrothermal vent sites along the northern East Pacific Rise. *Geochemistry, Geophysics, Geosystems*, *7*, Q03002. https://doi.org/10.1029/2005GC001094

Sclater, J. G., Jaupart, C., & Galson, D. (1980). The heat flow through oceanic and continental crust and the heat loss of the earth. *Reviews of Geophysics and Space Physics*, *18*(1), 269–311.

Seher, T., Crawford, W. C., Singh, S. C., & Cannat, M. (2010). Seismic layer 2A variations in the Lucky Strike segment at the Mid-Atlantic Ridge from reflection measurements. *Journal of Geophysical Research*, *115*, B07107. https://doi.org/10.1029/2009JB006783

Shank, T. M., Fornari, D. J., Von Damm, K. L., Lilley, M. D., Haymon, R. M., & Lutz, R. A. (1998). Temporal and spatial patterns of biological community development at nascent deep-sea hydrothermal vents along the East Pacific Rise. *Deep Sea Research Part II: Topical Studies in Oceanography*, *45*(1–3), 465–515.

Singh, S. C., Crawford, W. C., Carton, H., Seher, T., Combier, V., Cannat, M., et al. (2006). Discovery of a magma chamber and faults beneath a Mid-Atlantic Ridge hydrothermal field. *Nature*, *442*(7106), 1029–1032. https://doi.org/10.1038/nature05105.

Smith, D. K., & Cann, J. R. (1993). Building the crust at the Mid-Atlantic Ridge. *Nature*, *365*(6448), 707–715.

Sohn, R. A. (2007). Stochastic analysis of exit fluid temperature records from the active TAG hydrothermal mound (Mid-Atlantic Ridge, 26°N): 1. Modes of variability and implications for subsurface flow. *Journal of Geophysical Research*, *112*, B07101. https://doi.org/10.1029/2006JB004435

Sohn, R. A., Webb, S. C., & Hildebrand, J. A. (2004). Fine-scale seismic structure of the shallow volcanic crust on the East Pacific Rise at 9°50′N. *Journal of Geophysical Research*, *109*, B12104. https://doi.org/10.1029/2004JB003152

Stein, C. A., & Stein, S. (1992). A model for the global variation in oceanic depth and heatflow with lithospheric age. *Nature*, *359*, 123–128.

Stein, J. S., & Fisher, A. T. (2003). Observations and models of lateral hydrothermal circulation on young ridge flank: Numerical evaluation of thermal and chemical constraints. *Geochemistry, Geophysics, Geosystems*, *4*(3), 1026. https://doi.org/10.1029/2002GC000415

Theissen-Krah, S., Iyer, K., Rüpke, L. H., & Morgan, J. P. (2011). Coupled mechanical and hydrothermal modeling of crustal accretion at intermediate to Fast Spreading Ridges. *Earth and Planetary Science Letters*, *311*(3), 275–286.

Thomson, D. J. (1982). Spectrum estimation and harmonic analysis. *Proceedings of IEEE*, *70*(9), 1055–1096.

Tivey, M. A., & Johnson, H. P. (2002). Crustal magnetization reveals subsurface structure of Juan de Fuca Ridge hydrothermal vent fields. *Geology*, *30*(11), 979–982.

Tivey, M. K., Bradley, A. M., Joyce, T. M., & Kadko, D. (2002). Insights into tide-related variability at seafloor hydrothermal vents from time-series temperature measurements. *Earth and Planetary Science Letters*, *202*(3–4), 693–707.

Tolstoy, M., Cowen, J. P., Baker, E. T., Fornari, D. J., Rubin, K. H., Shank, T. M., et al. (2006). A sea-floor spreading event captured by seismometers. *Science*, *314*(5807), 1920–1922.

Tolstoy, M., Waldhauser, F., Bohnenstiehl, D. R., Weekly, R. T., & Kim, W. Y. (2008). Seismic identification of along-axis hydrothermal flow on the East Pacific Rise. *Nature*, *451*(7175), 181–184.

Van Ark, E., Detrick, R. S., Canales, J. P., Carbotte, S. M., Harding, A. J., Kent, G. M., et al. (2007). Seismic structure of the Endeavour segment, Juan de Fuca Ridge: Correlations with seismicity and hydrothermal activity. *Journal of Geophysical Research*, *112*, B02401. https://doi.org/10.1029/2005JB004210

Van der Kamp, G., & Gale, J. E. (1983). Theory of Earth tide and barometric effects in porous formations with compressible grains. *Water Resources Research*, *19*(2), 538–544. https://doi.org/10.1029/WR019i002p00538

Van Everdingen, D. A. (1995). Fracture characteristics of the sheeted dike complex, Troodos ophiolite, Cyprus: Implications for permeability of oceanic crust. *Journal of Geophysical Research*, *100*(B10), 19957–19972. https://doi.org/10.1029/95JB01575

Vera, E. E., & Diebold, J. B. (1994). Seismic imaging of oceanic layer 2A between 9°30′N and 10°N on the East Pacific Rise from two-ship wide-aperture profiles. *Journal of Geophysical Research*, *99*(B2), 3031–3041. https://doi.org/10.1029/93JB02107

Vera, E. E., Mutter, J. C., Buhl, P., Orcutt, J. A., Harding, A. J., Kappus, M. E., et al. (1990). The structure of 0- to 0.2-m.y.-old oceanic crust at 9°N on the East Pacific Rise from expanded spread profiles. *Journal of Geophysical Research*, *95*(B10), 15529–15556. https://doi.org/10.1029/JB095iB10p15529

Wagner, W., Cooper, J. R., Dittmann, A., Kijima, J., Kretzschmar, H.-J., Kruse, A., et al. (2000). The IAPWS industrial formulation 1997 for the thermodynamic properties of water and steam. *Journal of Engineering for Gas Turbines and Power*, *122*(1), 150–182.

Wang, K., & Davis, E. (1996). Theory for the propagation of tidally induced pore pressure variations in layered subseafloor formations. *Journal of Geophysical Research*, *101*(B5), 11483–11495. https://doi.org/10.1029/96JB00641

Wilcock, W. S. D., & Fisher, A. T. (2004). Geophysical constraints on the sub-seafloor environment near mid-ocean ridges. In W. S. D. Wilcock (Ed.), *The subseafloor biosphere at Mid-Ocean Ridges*, *Geophysical Monograph Series* (Vol. 144, pp. 51–74). Washington, DC: American Geophysical Union.

Wilcock, W. S. D., & McNabb, A. (1996). Estimates of crustal permeability on the Endeavour segment of the Juan de Fuca mid-ocean ridge. *Earth and Planetary Science Letters*, *138*(1–4), 83–91.

Williams, D. L., & Von Herzen, R. P. (1974). Heat loss from the Earth: New estimate. *Geology*, *2*(7), 327–328.

Winslow, D. M., Fisher, A. T., & Becker, K. (2013). Characterizing borehole fluid flow and formation permeability in the ocean crust using linked analytic models and Markov chain Monte Carlo analysis. *Geochemistry, Geophysics, Geosystems*, *14*, 3857–3874. https://doi.org/10.1002/ggge.20241

Wolery, T. J., & Sleep, N. H. (1976). Hydrothermal circulation and geochemical flux at mid-ocean ridges. *Journal of Geology*, *84*(3), 249–275.

Wright, D. J., Haymon, R. M., White, S. M., & Macdonald, K. C. (2002). Crustal fissuring on the crest of the southern East Pacific Rise at 17°15′–40′ S. *Journal of Geophysical Research*, *107*(B5), EPM 5-1–EPM 5–13. https://doi.org/10.1029/2001JB000544

Xu, G., Larson, B. I., Bemis, K. G., & Lilley, M. D. (2017). A preliminary 1-D model investigation of tidal variations of temperature and chlorinity at the Grotto Mound, Endeavour Segment, Juan De Fuca Ridge. *Geochemistry, Geophysics, Geosystems*, *18*, 75–92. https://doi.org/10.1002/2016GC006537

Xu, M., Pablo Canales, J., Carbotte, S. M., Carton, H., Nedimović, M. R., & Mutter, J. C. (2014). Variations in axial magma lens properties along the East Pacific Rise (9°30′N–10°00′N) from swath 3-D seismic imaging and 1-D waveform inversion. *Journal of Geophysical Research: Solid Earth*, *119*, 2721–2744. https://doi.org/10.1002/2013JB010730